

Decameter-sized Earth Impactors – II: A Bayesian Inference Approach to Meteoroid Ablation Modeling

Ian Chow^{1,2}, Peter G. Brown^{1,2}

¹Department of Physics and Astronomy, University of Western Ontario, 1151 Richmond St, London, N6A

3K7, Ontario, Canada

²Western Institute for Earth and Space Exploration, University of Western Ontario, Perth Drive, London, N6A 5B7, Ontario, Canada

Key Points:

- We develop a new method using dynamic nested sampling to estimate physical properties of meteoroids and asteroids from their light curves.
- Using our new method, we identify three object classes in a structurally varied decameter impactor population, ranging from weak to strong.
- Asteroids ranging from decimeter to decameter sizes both fragment in two distinct phases, but the latter do at much higher pressures.

Abstract

Small asteroids and large meteoroids frequently impact the Earth, though their physical and material properties remain poorly understood. When observed as fireballs in Earth's atmosphere, these properties can be inferred from their ablation and fragmentation behavior. The 2022 release of previously classified United States Government (USG) satellite sensor data has provided hundreds of new fireball light curves, allowing for more detailed analysis. Here we present a new Bayesian inference method based on dynamic nested sampling that can robustly estimate these objects' physical parameters from their observed light curves, starting from relatively uninformative, flat priors. We validate our method against seven USG sensor-observed fireballs with independent ground-based observations and demonstrate that our results are consistent with previous estimates. We then apply our technique to 13 decameter-size Earth impactors to conduct the most detailed population-level study of their structure and material strength to date. We identify three structurally distinct groups within the decameter impactors. The first group are primarily structurally homogeneous, weak objects which catastrophically disrupt below ~ 1.5 MPa. The second group are heterogeneous objects which progressively fragment starting from ~ 1 MPa typically up to $\sim 3-8$ MPa. The third group are strong aggregates which remain mostly intact until 9–10 MPa. Our results also suggest that decameter-size asteroids fragment in two distinct phases: an initial phase at $\sim 0.04-0.09$ MPa and a second at $\sim 1-4$ MPa. While decimeter- to meter-size objects typically lose most of their mass in the initial phase, larger decameter-size objects instead lose most of their mass in the second phase.

Plain Language Summary

Small asteroids frequently impact the Earth, but their strength and internal structure are still poorly understood. However, asteroids can be observed burning up in the atmosphere as bright fireballs, which can provide information on their structure. In 2022, data for hundreds of fireballs observed by United States Government (USG) satellite-based sensors were released to the public. Here we develop and validate a new statistical method to estimate the properties of impacting asteroids from their USG-recorded fireball light curves. We then apply this method to study the strength and structure of 13 decameter-size (roughly 10m-diameter) impactors, among the largest asteroids ever observed hitting the Earth. We identify three main types of impactors. The first group are uniformly weak and quickly disintegrate below about 1.5 MPa. The second group are made of material with a mix of strengths and gradually break up from about 1–8 MPa. The third group are relatively strong and remain intact until about 9–10 MPa. We also find large impactors break up in two stages, at about 0.04–0.09 MPa and 1–4 MPa. Smaller meteoroids typically lose most of their mass in the first stage, while the larger asteroids analyzed here instead do so in the second stage.

1 Introduction

Small asteroids ranging from 1–20 meters in size impact the Earth 35–40 times per year (P. Brown et al., 2002; Bland & Artemieva, 2006; P. G. Brown et al., 2013), often appearing as spectacular fireballs in the Earth's atmosphere. As most recovered meteorites originate from 1–20 meter-size asteroids (Borovička, 2015), this population in particular presents a unique opportunity to link data from fireball, telescopic and meteorite observations. The physical properties of these small asteroids have to date been poorly characterized at a population level, as they are often too small to be detected in space by telescopic surveys while also being comparatively rare as Earth impactors. However, the amount of data on the small asteroid population has grown significantly in recent years. In 2022, the U.S. Space Force publicly released decades of previously classified United States Government (USG) satellite sensor data on fireball events, includ-

ing light curves of intensity over time. This new USG sensor data has increased the number of known impactors of meter size or larger to over one thousand, allowing for much deeper analysis at a population level. Since 2019, the Geostationary Lightning Mapper (GLM) instrument onboard the Geostationary Operational Environmental Satellite (GOES) has also recorded light curves for thousands of bright bolides (McKinney et al., 2025), many of which are of meter size (Jenniskens et al., 2018).

Recent telescopic surveys have also allowed a number of meter-size asteroids to be observed in space before impact. In cases where such pre-impact telescopic observations are available, combined analyses of such asteroids, as near-Earth objects (NEOs) in space, fireballs in Earth's atmosphere and in select instances as recovered meteorites have allowed them to be characterized in great detail (e.g. Jenniskens et al., 2009, 2021; Geng et al., 2023; Clark et al., 2023; Spurný et al., 2024; Karefa et al., 2024; Gianotto et al., 2025; Ingebretsen et al., 2025; Egal et al., 2025). Upcoming surveys such as NEO Surveyor (Mainzer et al., 2023) and the Vera C. Rubin Observatory's Legacy Survey of Space and Time (LSST; Ivezić et al., 2019) are expected to discover over 100,000 NEOs each (Mainzer et al., 2023; Kurlander et al., 2025), with LSST expected to discover $\sim 1 - 2$ imminent Earth impactors per year (Chow et al., 2026, submitted).

The rapidly growing amount of data on these impactors thus presents a unique opportunity to conduct population-level analysis of their properties for the first time. Modern studies using light curve data to forward model and invert for the physical and material properties of specific meteorite-producing fireballs have typically proceeded by generating synthetic light curves by simulating the object's atmospheric ablation and fragmentation and then manually fitting the simulated light curve to observations by adjusting various model parameters. (e.g. Borovička, Tóth, et al., 2013; Wheeler et al., 2017; McMullan & Collins, 2019; McFadden et al., 2024). However, this manual fitting approach is labor-intensive, subject to parameter degeneracy and does not characterize uncertainties in these objects' inferred properties. Previous attempts to develop automated approaches for ablation modelling using genetic algorithms (Tárano et al., 2019; Henych et al., 2023) have seen only limited success for a small number of fireballs, require an initial manual solution to be found first and often need to be run numerous times per fireball to obtain a good fit to observations. Motivated by this recent release of USG sensor data, we therefore develop a novel automated Bayesian inference approach to meteoroid ablation modeling that uses dynamic nested sampling (Skilling, 2004, 2006; Higson et al., 2019) in conjunction with the semi-empirical fragmentation model of Borovička, Tóth, et al. (2013) to probabilistically estimate the physical and material properties of these fireballs solely from their light curves. Compared to previous manual fitting or genetic algorithm methods, our approach is capable of producing accurate fits from a single run under relatively uninformative flat priors and allows for robust uncertainty estimation in the physical properties of meteoroids. We validate our method against seven fireball events with USG light curves and for which detailed entry modeling has previously been conducted using independent ground-based observations, and demonstrate that our results are consistent with previous estimates. We then apply our method to 13 decameter-size Earth impactors previously identified in Chow and Brown (2025), where for all but one case (the 15 February 2013 Chelyabinsk bolide) only USG light curve data is available, to characterize the physical and material properties of these objects at a population level for the first time.

This paper is structured as follows: Section 2 introduces the USG sensor data used. Section 3 describes our light curve fitting procedure using the semi-empirical model and the nested sampling approach for parameter inference. In Section 4, we validate our nested sampling method against seven USG sensor-recorded fireballs for which entry modeling has been previously conducted using independent ground-based observations, and demonstrate that our results are generally consistent with previous estimates. We then apply our method in Section 5 to infer physical and material properties of 13 decameter-size

impactors previously identified in Chow and Brown (2025) and connect them to their dynamical origins. We discuss our results in Section 6. Finally, we summarize our conclusions and discuss future applications of the nested sampling method in Section 7.

2 Data

NASA’s Center for Near Earth Object Studies (CNEOS) Fireball and Bolide Database reports fireball events detected by satellite-based USG sensors, including light curves of fireball intensity as a function of time. From the only published information in the literature, the USG sensors observe in the optical passband from approximately 400–1100 nm at a sampling rate of 333 Hz and the total optical energy is converted from the sensor passband under the assumption that the overall spectral energy distribution of each fireball resembles a 6000 K blackbody (Tagliaferri et al., 1995). The total radiated energy and computed impact energy are recorded by CNEOS as well, and are generally consistent with energies determined through ground-based optical observations (Devillepoix et al., 2019), infrasound measurements (Gi & Brown, 2017) and common fireball detections by the GLM (Wisniewski et al., 2024). The heights of peak brightness also tend to be well estimated, with comparisons to ground-based observations suggesting errors are typically of order 2–3 km or less in most cases. Radiant information and speed are less accurately measured. This is discussed extensively in Chow and Brown (2025). We note that while fireball dynamics is a powerful tool for model constraints for smaller objects (Ceplecha et al., 1993), for the very large fireballs discussed here there is usually little to no observable deceleration prior to major fragmentation (and often little afterward) so the main information about the body is contained in the light curve. The light curves used for modeling in this work are primarily taken from the CNEOS database with the exception of the Chelyabinsk bolide, for which we use the light curve of P. G. Brown et al. (2013) as the USG sensor light curve is of poor quality.

3 Methods

In this section we describe our procedure for modeling the observed USG light curves. We use as our physical ablation model the semi-empirical model of meteoroid ablation and fragmentation developed by Borovička, Tóth, et al. (2013) and employ it in conjunction with dynamic nested sampling to estimate the posterior distribution of the model parameters.

3.1 Nested Sampling

Modern astronomy often requires inferring characteristics of physical models based on observational data. In recent decades, the rise of large astronomical datasets and concurrent advances in computational power for processing them have resulted in a paradigm shift for astrophysical inference problems, from traditional frequentist methods such as maximum likelihood estimation (Fisher, 1922) to Bayesian methods which aim to estimate the posterior distribution of a set of model parameters given some prior knowledge and observed data.

Under a Bayesian framework, the posterior distribution of a vector of parameters Θ for a given model M conditioned on observed data D is given by Bayes’ theorem

$$P(\Theta|D, M) = \frac{P(D|\Theta, M) P(\Theta|M)}{P(D|M)} \quad (1)$$

where $P(D|\Theta, M) = \mathcal{L}(\Theta)$ is the likelihood function, $P(\Theta|M) = \pi(\Theta)$ is the prior and $P(D|M) = \mathcal{Z}$ is the Bayesian evidence (or marginal likelihood), a term which quantifies how well the data supports the specific model. For complicated, high-dimensional models, such as those used for simulating meteoroid ablation, the posterior is often an-

alytically intractable, necessitating the use of numerical methods to estimate the posterior using a finite number of weighted points.

One such method is nested sampling (Skilling, 2004, 2006), which estimates both the Bayesian evidence as well as the posterior distribution. Nested sampling works by dividing the posterior distribution into nested “slices” with contours of constant likelihood and sequentially sampling from each slice before combining the samples (with appropriate weights) to estimate the overall posterior. Nested sampling is effective for high-dimensional problems with multimodal posteriors, where other sampling techniques popular for astrophysical inference such as Markov Chain Monte Carlo (MCMC; Goodman & Weare, 2010; Foreman-Mackey et al., 2013) often perform poorly. This is particularly salient for meteoroid ablation modelling, where previous studies have typically noted that the manually determined solution is not unique and can often be reproduced by many different physically reasonable fragment sequences or parameters (e.g. Borovička, Tóth, et al., 2013; Borovička et al., 2017, 2019; Henych et al., 2023).

Dynamic nested sampling (Higson et al., 2019) is a modification of nested sampling that adaptively allocates live points during the sampling process to favor sampling particular regions of parameter space. By increasing the number of points in regions where the majority of the posterior “mass” is located and reducing the number of points elsewhere, dynamic nested sampling can produce a more precise estimate for the posterior distribution at the cost of a less precise estimate for the Bayesian evidence. In this work we are primarily interested in the posterior distribution of the model parameters rather than the evidence and as such adopt the dynamic nested sampling paradigm for inference throughout.

3.2 Meteoroid Ablation Model

We use the semi-empirical model of meteoroid ablation and fragmentation first introduced by Borovička, Tóth, et al. (2013) which is grounded in earlier work that focused on fireball gross fragmentation dynamics and ablation (Ceplecha et al., 1993) and uses the modern synthesis for intrinsic/apparent ablation and luminous efficiency described in Ceplecha and Revelle (2005). As the name implies, it is an empirically adapted version of single-body ablation informed by precise observations of fireballs, with particular focus on describing fireball fragmentation as a physical process with model outputs tuned to be directly comparable to direct measurements of fireballs. In the model, the positions of fragmentation points can be adjusted as required, with each fragmentation producing either monolithic single-body fragments, dust, or eroding fragments which are major fragments that gradually release dust over a period of time after ejection from the main body. The individual light curves produced by the ablation of each fragment or dust particle are then computed and summed to form the total light curve for the object. Atmospheric densities are taken from the empirical NRLMSISE-00 model of Picone et al. (2002), evaluated at the time and location of each fireball. More details of the semi-empirical model are given in O. Popova et al. (2019) and Borovička et al. (2020). All light curve modeling in this paper is conducted using the `MetSim` software (Vida et al., 2023).

Our model fits involve finding suitable physical parameters which reproduce the observed light curve as a function of height. In our fitting process, we first manually select one or more approximate fragmentation heights H_j for each impactor based on the shape of the USG lightcurve. For the validation cases, we associate these USG-based estimates with the major fragmentation points identified in previous studies. To simplify the model, we assume that every fragmentation produces an eroding fragment, as the release of single-body fragments or dust can be approximated as end member cases by using a very low or very high erosion coefficient, respectively. Each fragment is then parameterized by its fragmentation height h , mass as a percentage of the initial meteoroid mass m_{frag} , erosion coefficient η , grain minimum mass m_{lower} and grain maximum mass

m_{upper} . The initial meteoroid mass m_{init} is also included as a free parameter in our model. We adopt a fixed initial bulk density of 1500 kg m^{-3} based on other estimates of NEO bulk densities (see Section 2 of Chow & Brown, 2025, and references therein) and a fixed grain density of 3500 kg m^{-3} appropriate for chondritic meteorites (Flynn et al., 2018). While we recognize there is some variance in the bulk density of these impactors, it is difficult to quantify. However, as discussed in Section 6.1, we empirically find that this uncertainty in the bulk density does not significantly affect the results of our analysis.

For each impactor, we use a fixed initial velocity v based on the USG-reported entry velocity and a fixed luminous efficiency τ based on the optical energy- τ function given in P. Brown et al. (2002). Finally, we also use a fixed shape parameter of $\Gamma A = 0.8$ following Borovička et al. (2020), a mass distribution index of $s = 2.5$ and an ablation coefficient of 0.005 kg MJ^{-1} across all fragments and all fireballs as found to be representative for chondritic meteoroids (Ceplecha & Revelle, 2005; Borovička et al., 2020).

The free parameters determining the light curve data for a model with k fragmentation points are thus $\Theta = \{m_{\text{init}}\} \cup \{m_{\text{frag}_j}, \eta_j, m_{\text{lower}_j}, m_{\text{upper}_j}, h_j\}_{j=1}^k$. Assuming Gaussian uncertainty in the observations, the log-likelihood $\ln \mathcal{L}$ of a given set of parameters Θ is then written as

$$\ln \mathcal{L}(\Theta) = - \sum_{i=1}^N \left(\frac{(L_i - \bar{L}_i(\Theta))^2}{2\sigma_i^2} + \ln \sqrt{2\pi\sigma_i^2} \right), \quad (2)$$

where L_i denotes the i th observed luminosity sample, σ_i^2 denotes the corresponding measurement uncertainty, and $\bar{L}_i(\Theta)$ denotes the simulated luminosity from the ablation model at the height of observation.

The posterior distribution of the free parameters Θ is then estimated using dynamic nested sampling. In our model, the fragments' grain minima m_{lower_j} , grain maxima m_{upper_j} , and the initial meteoroid mass m_{init} are parameterized by their logarithms $\log_{10} m_{\text{lower}_j}$, $\log_{10} m_{\text{upper}_j}$ and $\log_{10} m_{\text{init}}$ respectively. We adopt uniform priors for all model parameters over their respective intervals, summarized in Table 1. Our priors are relatively uninformative and are chosen to ensure that the full range of physically reasonable parameter values are contained. Note that the lower bound for the grain maximum is set so it cannot be smaller than the grain minimum. The bounds on the fragmentation heights h_j are set based on the manually selected fragmentation heights H_j as the smaller of 5 kilometers or half the vertical distance to the previous or next manually selected fragmentation point (if applicable), to ensure that fragmentation heights are always in strictly descending order.

The USG sensor data does not include observational uncertainties. We therefore estimate a fixed measurement uncertainty of $\sigma_i = 1.2 \times 10^{10} \text{ W ster}^{-1}$ for all USG observations in this paper, based on the detection limit of USG sensors at magnitude ~ -16.5 assuming a bolometric power of 3030 W at zero magnitude. For each event, the dynamic nested sampling is then conducted with the `dynesty` (Speagle, 2020; Koposov et al., 2024) software package using 1000 live points and the random-slice sampling strategy (Neal, 2003; Handley et al., 2015b, 2015a), with the stopping condition and other hyperparameters set to default values.

4 Validation Against Ground-Based Observations

Here we validate our method against all seven fireballs (listed in chronological order) for which detailed light curve modelling has previously been conducted using independent ground-based observations, to compare the range of the parameter values derived from our nested sampling-based method to estimates of previous works. For each event, the maximum log-likelihood solution and the 5%, 50% (median) and 95% quan-

Parameter	Lower Bound	Upper Bound
$\log_{10} m_{\text{init}}$ (\log_{10} kg)	2	8
For jth fragment:		
m_{frag_j} (% of m_{init})	0	100
η_j ($\text{s}^2 \text{ km}^{-2}$)	0.01	10
$\log_{10} m_{\text{lower}_j}$ (\log_{10} kg)	-5	2
$\log_{10} m_{\text{upper}_j}$ (\log_{10} kg)	$\max(\log_{10} m_{\text{lower}_j}, -4)$	3
h_j (km)	$\max(H_j - 5, \frac{H_j + H_{j-1}}{2})$	$\min(H_j + 5, \frac{H_{j+1} + H_j}{2})$

Table 1. Prior bounds for all free model parameters used for nested sampling. We adopt uniform priors over all model parameters with the specified lower and upper bounds. The lower bound for the fragment grain maximum m_{upper_j} is imposed based on the chosen grain minimum m_{lower_j} (as the maximum must be greater than the minimum), and the bounds on the fragmentation heights h_j are set based on H_j , the *manually* selected fragmentation heights, to ensure that they remain in strictly descending order.

tiles of the 1D posterior distributions for several relevant physical quantities of the object derived from nested sampling are recorded. These quantities are the initial object mass m_{init} , the dynamic pressure at the main fragmentation point P_{main} , the mass released at the main fragmentation point m_{main} , the peak dynamic pressure experienced P_{peak} , and the mass remaining at peak dynamic pressure m_{peak} . Note that the choice of luminous efficiency model is generally the main driver scaling differences in initial mass. Here we adopt the empirical integral luminous efficiency model from P. Brown et al. (2002) as it was calibrated using USG-recorded events from USG sensors. This model sets luminous efficiency to be independent of mass and velocity, depending only on the initial optical energy of the fireball. The more detailed luminous efficiency model of Borovička et al. (2020), which is part of the semi-empirical model framework, has much better validation at small masses and offers more precise overall measurements (including terms for velocity and mass) but for much smaller fireballs than considered here. We summarize our results in Table 2 and discuss each event individually in the following sections.

4.1 Tagish Lake

The Tagish Lake meteorite fell in Canada on 18 January 2000. It was accompanied by a bright fireball detected by USG sensors, seismic and infrasonic stations and recorded by eyewitnesses on video (P. G. Brown et al., 2002; Hildebrand et al., 2006). The pre-impact mass of the object was estimated to be between 33–100 tons by P. G. Brown et al. (2002) using several different methods. Modeling the USG sensor light curve with the gross fragmentation model of Ceplecha et al. (1993) (a precursor to the semi-empirical model), P. G. Brown et al. (2002) placed the first major burst point at a height of 37 km under a dynamic pressure of 0.7 MPa. The meteoroid reached its peak dynamic pressure of 1.2 MPa at a height of ~ 30.8 km. While fragment masses are not reported, P. G. Brown et al. (2002) also estimated that ~ 26 tons of the original 56-ton mass remained at the 37-km burst point (which we take as the mass released at the main fragmentation) and that ~ 2.2 tons remained at peak dynamic pressure.

In this work we model the USG light curve as seen in Figure 1a), focusing on the two large fragmentations at 37 and 32 km altitude identified by P. G. Brown et al. (2002) and visible in the USG light curve. The posterior parameter estimates from our nested

Event	m_{init} (kg)			P_{main} (MPa)			m_{main} (% of m_{init})			P_{peak} (MPa)			m_{peak} (% of m_{init})		
	5%	50%	95%	5%	50%	95%	5%	50%	95%	5%	50%	95%	5%	50%	95%
Tagish Lake	33000 – 100000			0.7			46			1.2			3.9		
(1)	95000	98000	100000	0.9	1.0	1.0	41	47	53	3.0	3.1	5.2	1.9	2.5	3.6
This work max. log \mathcal{L}															
Morávka	230 – 11000			4.3			48			5.0			18		
(2)	3000	3000	5100	2.6	3.9	4.5	19	38	80	5.5	8.7	11	11	26	39
This work max. log \mathcal{L}															
Park Forest	7000 – 21000			5.38 – 6.99			63			14.0			0.84		
(3)	13000	13000	15000	6.18	6.26	6.35	79	87	88	8.00	8.67	10.6	0.92	3.8	11
This work max. log \mathcal{L}															
Košice	1200 – 11000			0.97			91			5.9			0.52		
(4)	17000	17000	22000	0.85	0.91	1.00	79	97	99	3.5	5.9	15	0.086	1.2	10
This work max. log \mathcal{L}															
Romania	3000 – 6800			1.0			90			3.0			~ 0		
(5)	13000	12000	15000	0.9	1.0	1.1	60	79	86	20	25	27	0.56	0.87	1.7
This work max. log \mathcal{L}															
Sarıçek	780 – 2700			1.00			not reported			3.99			1.6		
(6)	2300	2300	2900	1.29	1.42	1.49	44	55	91	4.11	6.11	9.73	1.6	2.9	7.7
This work max. log \mathcal{L}															
Flensburg	10000 – 22000			0.7			68			2.0			3		
(7)	18000	18000	19000	0.5	0.7	0.7	54	77	97	2.7	7.2	8.8	3	10	10
This work max. log \mathcal{L}															
This work quantiles															

Table 2. The maximum log-likelihood fit and nested sampling posterior quantiles for physical parameters of seven USG sensor-recorded fireball events compared to previous parameter estimates derived using independent ground-based observations, with corresponding references provided. The parameters are the initial mass m_{init} , dynamic pressure at main fragmentation P_{main} , mass released at main fragmentation m_{main} , peak dynamic pressure P_{peak} and mass remaining at peak dynamic pressure m_{peak} . These seven events represent all fireballs both observed by USG sensors and for which detailed light curve modeling has previously been conducted using the independent observations. Computed results are rounded to the same number of significant digits reported by previous studies.

References: (1) P. G. Brown et al. (2002) and Hildebrand et al. (2006); (2) Neder et al. (2001), Borovicka, Weber, et al. (2003), Borovicka, Spurný, et al. (2003) and Borovicka and Kalenda (2003); (3) P. Brown et al. (2004); (4) Borovička, Tóth, et al. (2013); (5) Borovička et al. (2017); (6) Unsalan et al. (2019); (7) Borovička et al. (2021).

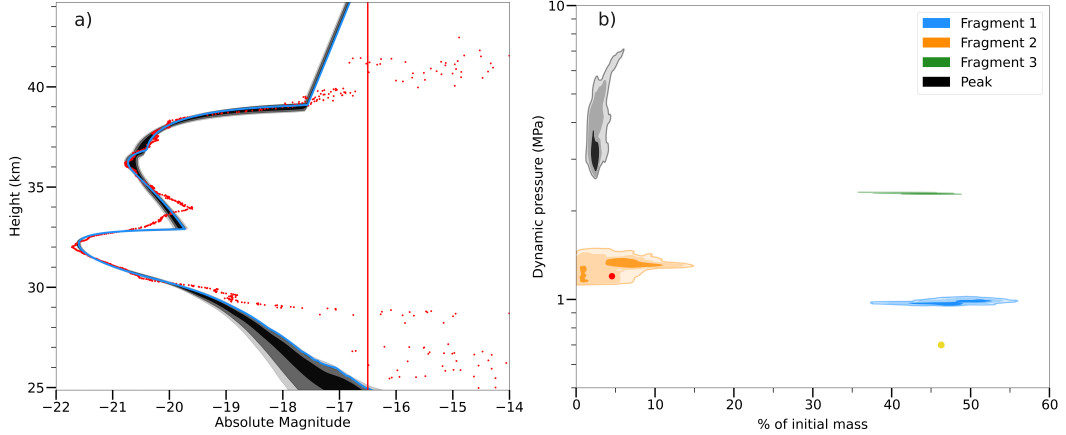


Figure 1. a): The model light curve of intensity versus height plotted over the USG sensor-recorded fireball light curve (red dots) for the 18 January 2000 Tagish Lake meteorite-producing fireball. Here the black shaded regions illustrate the 1σ , 2σ and 3σ distributions for the light curve solutions derived from nested sampling. The maximum log-likelihood solution obtained by nested sampling is plotted as the blue line. The intensity is given in units of absolute stellar magnitudes assuming a bolometric power of 3030 W at zero magnitude. The detection limit of USG sensors at absolute magnitude -16.5 is marked by the vertical red line. b): The marginal 2D posterior distributions of dynamic pressure against mass released for each fragmentation point (colors) identified from the USG light curve and mass remaining at peak dynamic pressure (black). Contours show the 1σ , 2σ and 3σ bounds of the posterior distributions. Also marked on the plot are the dynamic pressure vs. mass released at the main fragmentation point (yellow dot) and at peak dynamic pressure (red dot) previously estimated by P. G. Brown et al. (2002).

sampling-based model largely concur with previous results, with the main-burst dynamic pressure being less than a factor of two higher and peak dynamic pressure being a factor of three higher than the values estimated by P. G. Brown et al. (2002).

4.2 Morávka

The daytime Morávka meteorite fall in the eastern Czech Republic on 6 May 2000 was accompanied by a bright fireball detected by USG sensors, seismic and infrasonic stations and by several serendipitous casual video recordings (Borovicka, Spurný, et al., 2003). The latter provided details of fragmentation, lateral fragment velocity spread and mass loss as a function of height. Neder et al. (2001) and Borovicka and Kalenda (2003) determined the pre-impact mass of the object using several different techniques, producing a range from 230–11000 kg with a best overall estimate of 1500 ± 500 kg (Borovicka & Kalenda, 2003). Dynamical modeling of observed fragments by Borovicka, Weber, et al. (2003) using the video footage found that significant low-altitude gross fragmentation began at a height of 32.3 km under dynamic pressure of 4.3 MPa. At this point, the object had already been broken into four large fragments of masses 142, 114, 106 and 77 kg (determined based on their observed deceleration) which were released unobserved at higher altitude.

The four initial fragments tracked by Borovicka, Weber, et al. (2003) then each fragmented again between 32.3 and 29.3 km, with the overall peak dynamic pressure of 5.0 MPa reached by the 77-kg fragment at 29.3 km. Smaller fragmentation events were then subsequently tracked by Borovicka, Weber, et al. (2003) down to 24.0 km. The fraction

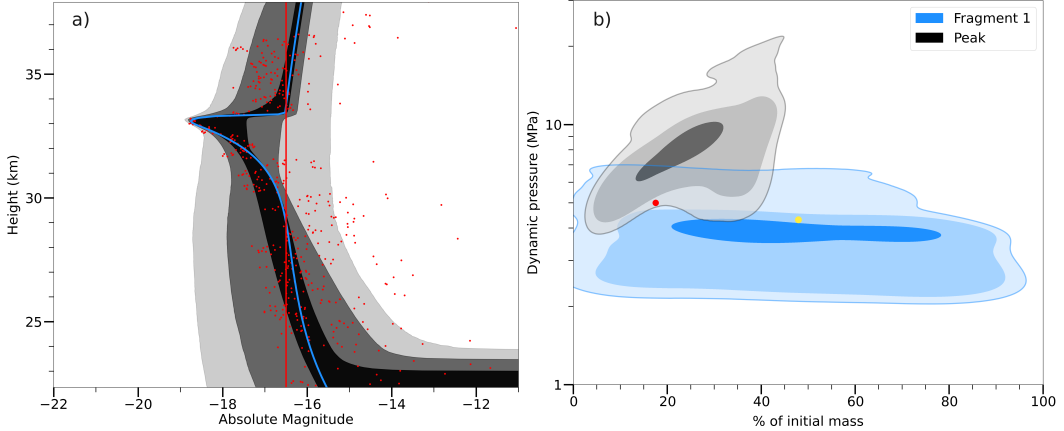


Figure 2. **a)**: The observed light curve and corresponding model fit for the 6 May 2000 Morávka fireball, similar to Figure 1a). Evidence of extended luminosity possibly produced by dust left behind by the bolide after its final fragmentation is visible as an inflection in the light curve at ~ 31 km. **b)**: Comparison of the posterior distributions for dynamic pressure against mass released at the main fragmentation and mass remaining at peak dynamic pressure to previous estimates by Borovicka, Weber, et al. (2003), similar to Figure 1b).

of overall mass of the four initial fragments represented by the 77-kg fragment is taken as our estimate for mass remaining at peak dynamic pressure.

Here we instead model the USG light curve using only a single fragmentation event at ~ 33 km where a large flare can be seen in Figure 2a), corresponding to the onset of fragmentation as identified by Borovicka, Weber, et al. (2003). We do not model the other fragmentations as the rest of the USG light curve is close to the detection limit and consequently of low fidelity. Comparing our nested sampling-based fit with the USG sensor data to the dynamical modeling results of Borovicka, Weber, et al. (2003), we find that our results compare very favorably overall, with only our inferred peak dynamic pressure being higher than the 5.0 MPa estimated by Borovicka, Weber, et al. (2003). We suggest this may be due to residual luminosity detected by USG sensors from the bolide's sunlit stationary trail being mapped to light production at apparently lower altitudes. This can be seen in the Figure 2a) light curve but is not a real feature, as evidenced by the dynamical modeling of Borovicka, Weber, et al. (2003).

4.3 Park Forest

The Park Forest meteorite fell in the United States on 27 March 2003. It was accompanied by a bright fireball detected by USG sensors, seismic, infrasonic and acoustic microphones and by casual videos (P. Brown et al., 2004). Mass estimates with several different techniques by P. Brown et al. (2004) yielded a pre-impact mass for the object ranging between 7000–21000 kg with a nominal best estimate of 11000 ± 3000 kg. Using the gross fragmentation model of Ceplecha et al. (1993), P. Brown et al. (2004) also analyzed a fused light curve of USG sensor and ground-based video observations to determine fireball fragmentation behavior. They identified three large fragmentation points at 37, 29 and 22 km, with the main burst occurring at 29 km under a dynamic pressure of 7 MPa (possibly overestimated by 20–30%). P. Brown et al. (2004) also determined using the gross fragmentation model that the overall peak dynamic pressure of 14 MPa was reached at a height of ~ 21.3 km, where ~ 92.5 kg of the 11000 kg initial mass remained.

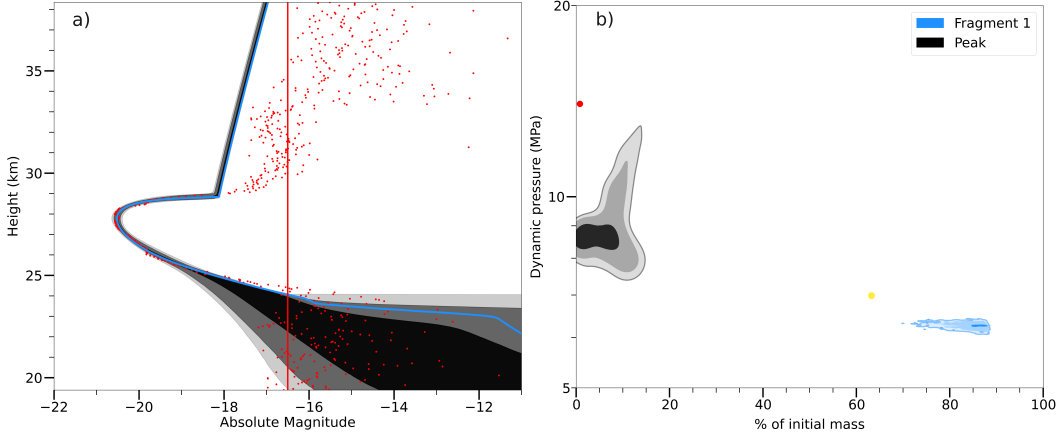


Figure 3. a): The observed light curve and corresponding model fit for the 27 March 2003 Park Forest fireball, similar to Figure 1a). b): Comparison of the posterior distributions for dynamic pressure against mass released at the main fragmentation and mass remaining at peak dynamic pressure to previous estimates by P. Brown et al. (2004), similar to Figure 1b).

Here we model the USG light curve considering only the main burst at 29 km identified by P. Brown et al. (2004) and shown in Figure 3a), as the other two fragmentations occurred close to the USG sensor detection limit. Our nested sampling-based results for initial mass, dynamic pressure at main burst, and mass remaining at peak dynamic pressure are consistent with the estimates reported by P. Brown et al. (2004). The mass released at the main fragmentation is somewhat larger than previous nominal estimates by P. Brown et al. (2004), while the main-burst and peak dynamic pressures are somewhat smaller. The former discrepancy is likely because we do not consider the first large fragmentation at 37 km identified by P. Brown et al. (2004) in this work (where some mass would have been released), while the latter could be due to differences between the simpler gross fragmentation model used by P. Brown et al. (2004) in their analysis compared to the semi-empirical model of Borovička, Tóth, et al. (2013) employed in this work.

4.4 Košice

The Košice meteorite fall in eastern Slovakia on 28 February 2010 was accompanied by a bright fireball detected by USG sensors, radiometers of the ground-based European Fireball Network (EN), seismic and infrasonic stations, and surveillance cameras in Hungary (Borovička, Tóth, et al., 2013). Using the radiometric light curve, Borovička, Tóth, et al. (2013) determined a pre-impact mass of 3500 kg citing a factor of 3 uncertainty in this value. The main fragmentation occurred at a height of 38.9 km under dynamic pressure of 0.97 MPa. Borovička, Tóth, et al. (2013) also identified a second large fragmentation of the main body at 29.3 km. The peak dynamic pressure of 5.9 MPa was reached by an 18.1-kg fragment at 21.6 km.

In our model for this work only the two fragmentation points at 38.9 and 29.3 km are considered as they are clearly visible in the USG sensor light curve shown in Figure 4a). We combine the three smaller fragmentations of previously released fragments at 36.6, 34.8 and 33.7 km identified by Borovička, Tóth, et al. (2013) into the main fragmentation at 38.9 km here, totaling 3175 kg released from the initial mass of 3496 kg. Our posterior parameter estimates are consistent with the results obtained by Borovička, Tóth, et al. (2013) with the exception of the initial mass, which we find to be substan-

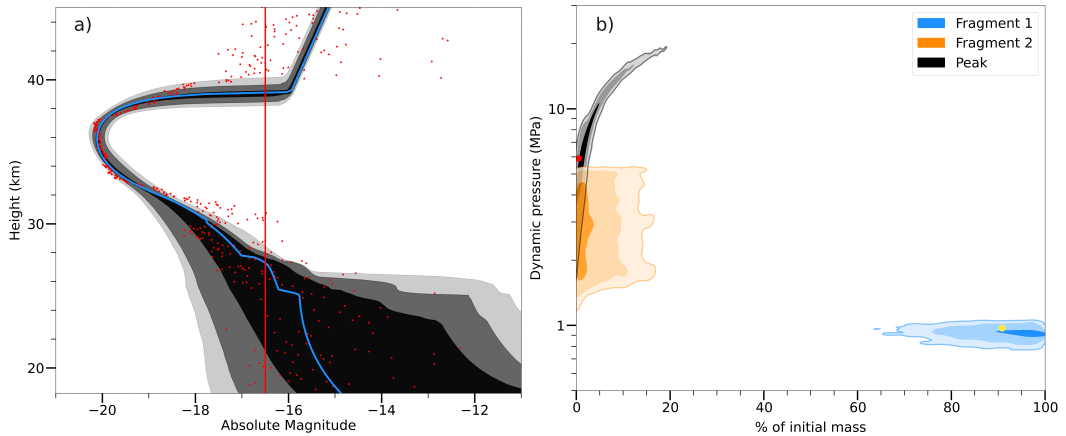


Figure 4. a): The observed light curve and corresponding model fit for the 28 February 2010 Košice fireball, similar to Figure 1a). b): Comparison of the posterior distributions for dynamic pressure against mass released at the main fragmentation and mass remaining at peak dynamic pressure to previous estimates by Borovička, Tóth, et al. (2013), similar to Figure 1b).

tially larger in part because the corrected USG lightcurve is almost two magnitudes brighter than the inferred peak brightness from ground-based detectors. However, as noted by Borovička, Tóth, et al. (2013), the ground-based brightness is uncertain to roughly one stellar magnitude so this difference is not unexpected.

4.5 Romanian Fireball

A superbolide occurred over central Romania on 7 January 2015, from which no meteorites were recovered (Borovička et al., 2017). The fireball was observed by USG sensors, EN all-sky cameras and radiometers located in the Czech Republic and Slovakia, and surveillance cameras in Romania. Analysis by Borovička et al. (2017) determined a pre-impact mass of ~ 4500 kg with uncertainty of $\pm 50\%$. Modeling the radiometric light curve, Borovička et al. (2017) identified an initial flare releasing 30 kg of mass at 53.5 km, followed by severe fragmentation beginning at 48 km height and dynamic pressure of 0.9 MPa and occurring almost continuously down to 42 km, releasing a total of 4050 kg. The remaining body started eroding at 40.9 km and completely disintegrated into dust around 38 km after reaching a peak dynamic pressure of 3.0 MPa.

Here we model the bolide considering the initial flare at 53.5 km and the main fragmentation at 48 km identified by Borovička et al. (2017) and apparent in the USG light curve. The subsequent individual fragmentations are all combined into a single fragmentation at ~ 46 km to simplify the model. The USG light curve and our resulting fit can be seen in Figure 5a). Our estimate for the dynamic pressure and mass released at the main fragmentation point match well with the values estimated by Borovička et al. (2017), while our peak dynamic pressure is an order of magnitude higher. Similar to Morávka, this discrepancy is likely due to ongoing trail emission being detected by USG sensors mapping to apparent (but non-existent) low-altitude luminosity as seen in Figure 5a). We model this extended light for consistency here (treating the USG light curve as the only information we have for this event) but Borovička et al. (2017) do not, as they recognized this “shelf” of persistent luminosity as being due to the fixed bolide trail which they were able to directly resolve.

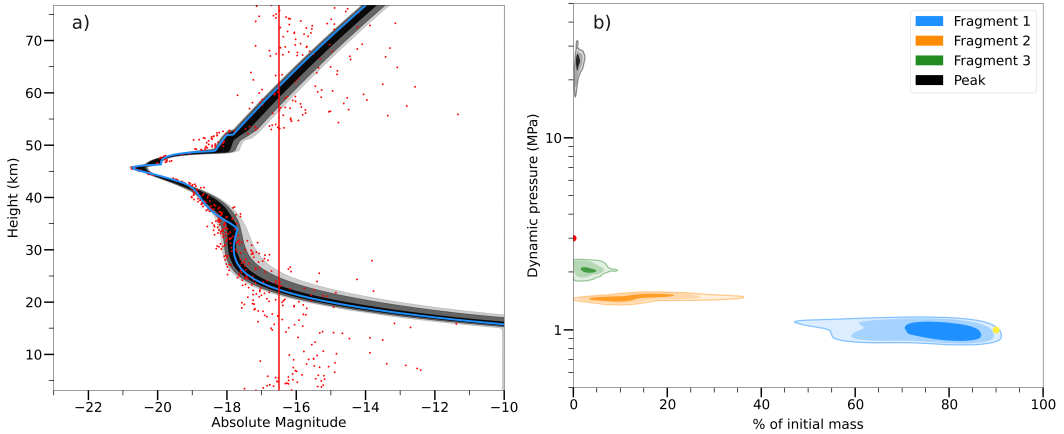


Figure 5. a): The observed light curve and corresponding model fit for the 7 January 2015 Romanian superbolide, similar to Figure 1a). Similar to Figure 2a), extended luminosity appears as an inflection in the light curve at ~ 35 km. b): Comparison of the posterior distributions for dynamic pressure against mass released at main fragmentation and mass remaining at peak dynamic pressure to previous estimates by Borovička et al. (2017), similar to Figure 1b).

4.6 Sarıçek

The Sarıçek meteorite fall in Turkey on 2 September 2015 was accompanied by a bright fireball detected by USG sensors, seismic sensors, and security cameras in Turkey (Unsalan et al., 2019). Analysis by Unsalan et al. (2019) determined the object's pre-impact diameter to be 1.0 ± 0.2 m, which when combined with the 2910 ± 20 kg m $^{-3}$ bulk density of recovered meteorites yields a pre-impact mass estimate of 775 – 2651 kg. Using the triggered progressive fragmentation model of ReVelle (2004) to model the security camera light curve, Unsalan et al. (2019) identified flares at heights 36.4, 33.0, 31.0, and 27.4 km, with dynamic pressures of 1.00 MPa at the first (and largest) flare and 3.99 MPa at the last flare, where the object completely disrupted. We take this last value to be the peak dynamic pressure and the total mass of 24.78 kg recovered meteorites (Unsalan et al., 2019) to be an estimate for the mass remaining at peak dynamic pressure. The masses released at each fragmentation are not reported.

In this work we model the Sarıçek bolide light curve as having four fragmentation events as evidenced by the USG light curve. These are common with the four flares identified by Unsalan et al. (2019). The USG light curve and our resulting fit obtained using nested sampling is shown in Figure 6a). We note that our dynamic pressure at the main fragmentation is somewhat higher than that of Unsalan et al. (2019), while our other estimates are generally consistent. This discrepancy is likely due to the difference in the height of peak brightness reported by USG sensors (39.8 km) compared with that determined via the security camera footage by Unsalan et al. (2019) (36.2 km); the four flares are instead at heights ~ 44.9 km, ~ 40.5 km, ~ 38.6 km, and ~ 35.0 km in our model.

4.7 Flensburg

The Flensburg C1-ungrouped meteorite fall occurred in northern Germany on 12 September 2019 (Bischoff et al., 2021; Borovička et al., 2021). The associated daytime bolide was observed by USG sensors, the ground-based AllSky6 meteor observing camera system (Hankey et al., 2020) and dashboard cameras. Borovička et al. (2021) obtained a pre-impact mass range of 10,000–22,000 kg for the object. The lower mass estimate

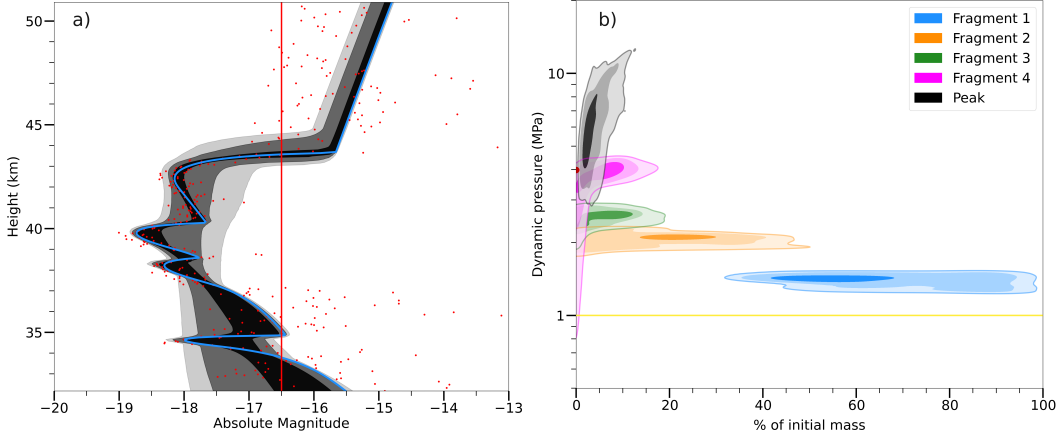


Figure 6. **a)**: The observed light curve and corresponding model fit for the 2 September 2015 Sariçek fireball, similar to Figure 1a). **b)**: Comparison of the posterior distributions for dynamic pressure against mass released at main fragmentation and mass remaining at peak dynamic pressure to previous estimates by Unsalan et al. (2019), similar to Figure 1b). Note that the estimated dynamic pressure at the main fragmentation point by Unsalan et al. (2019) is indicated by a line rather than a dot in this case as the released mass is not reported.

was derived using the USG-reported impact energy, while the upper estimate was derived by fitting an approximate ground-based light curve normalized to the total USG sensor energy with the semi-empirical model of Borovička, Tóth, et al. (2013) using a similar method to that of Borovička et al. (2019) for the CM2 carbonaceous chondrite Maribo. Based on detailed modeling of the AllSky6 and dashcam light curves, Borovička et al. (2021) also identified the main fragmentation of the object at a height of 45.5 km and dynamic pressure of 0.7 MPa, releasing 15000 kg from the 22000 kg main body. This was followed by smaller fragmentations at 42.5 and 37 km, the latter of which saw the object reach its peak dynamic pressure of 2.0 MPa where an estimated $\sim 3\%$ of initial mass remained.

We model the light curve here considering only the two fragmentations found by Borovička et al. (2021) at 45.5 and 42.5 km, as the final fragmentation at 37.5 km is not visible in the USG light curve (shown in Figure 7a)). Our inferred estimates of initial mass, dynamic pressure and mass released at the main fragmentation point from the USG sensor light curve are broadly consistent with previous work by Borovička et al. (2021), while our inferred peak dynamic pressure and mass remaining at peak pressure are again substantially higher. As with the Morávka and the Romanian bolides, this may be due to lingering emission in the daytime sky producing an apparent low-altitude luminous trail (as seen in Figure 7a)) detected by the USG sensors.

4.8 Discussion

Overall, we find that for these seven validation bolide cases our initial mass estimates are similar to those estimated in the literature, noting that differences in the USG versus ground-based light curves and assumptions in luminous efficiency can easily produce deviations of a factor of several in the initial mass. For those fireballs for which detailed modelling was available, we find that our dynamic pressure where the majority of the mass is released is most similar to our results. We therefore suggest that our method is most robust at estimating the dynamic pressure and associated mass loss at primary fragmentation.

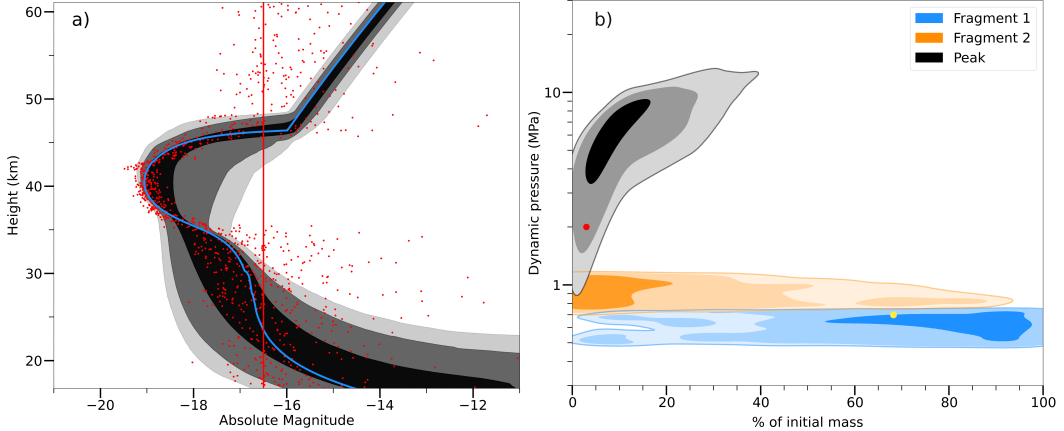


Figure 7. a): The observed light curve and corresponding model fit for the 12 September 2019 Flensburg fireball, similar to Figure 1a). Similar to Figure 2a), extended luminosity appears as an inflection in the light curve at ~ 35 km. b): Comparison of the posterior distributions for dynamic pressure against mass released at main fragmentation and mass remaining at peak dynamic pressure to previous estimates by Borovička et al. (2021), similar to Figure 1b).

We note that for the Morávka, Romania and Flensburg bolides, our inferred peak dynamic pressure is substantially higher than previous estimates. This is likely due to the common observations by USG sensors of an extended, stationary luminous trail produced by optically thick hot vapor and/or residual dust (Borovička et al., 2017). In all three of these cases, this feature appears as an inflection in the light curve after the main or final fragmentation. For daytime fireballs such as Morávka and Flensburg, reflected sunlight from the debris cloud may also be a contributor as this effect has been previously identified as causing long “tails” in USG sensor light curves (Tagliaferri et al., 1995).

A major result of these comparisons is that caution should be exercised in fitting or interpreting USG sensor light curves past their point of peak brightness. It appears in many cases that extended emission is a common feature and may result in inflated peak dynamic pressures or total optical energies.

5 Decameter Impactors

Here we apply our nested sampling method to 13 decameter-size impactors, consisting of all impactors identified in Table 1 of Chow and Brown (2025) with the exception of the 7 February 2022 South Atlantic fireball, which is excluded from our analysis. We excluded this event as the USG light curve shows an unphysical rise in post-peak brightness consistent with a signature of contamination from a persistent trail. This suggests its energy is overestimated. Indeed, infrasound records from six stations which show a clear signal from the bolide produce an average period of 6.8 sec. The multi-station average period-yield relationship of Ens et al. (2012) therefore suggests a source yield estimate below 3 kilotons of TNT ($1 \text{ kT TNT} = 4.184 \times 10^{12} \text{ J}$), further supporting our choice to remove this event from consideration as it is likely well below the 7.5m diameter threshold of our survey.

As for the validation events, the maximum log-likelihood solution as well as the 5%, 50% and 95% quantiles of the 1D posterior distributions of relevant physical parameters for each event are recorded. These results are summarized in Table 3. Figure 8a) shows an example light curve for one of the decameter impactors (the 1 February 1994 Mar-

UTC Date (YYYY-MM-DD)	m_{init} (10^5 kg)			P_{main} (MPa)			m_{main} (% of m_{init})			P_{peak} (MPa)			m_{peak} (% of m_{init})			Structural Class
	5%	50%	95%	5%	50%	95%	5%	50%	95%	5%	50%	95%	5%	50%	95%	
1994-02-01 max. log \mathcal{L}	4.71			13.8			36.8			94.0			5.82			Heterogeneous
1994-02-01 quantiles	4.54	4.74	4.92	13.5	14.2	14.5	22.1	35.8	41.1	79.6	93.2	103	3.61	5.69	7.47	
1999-01-14 max. log \mathcal{L}	4.08			0.0666			65.7			5.48			0.0307			Weak Homogeneous
1999-01-14 quantiles	3.90	4.06	4.25	0.0501	0.0666	0.0939	56.8	70.3	81.5	5.20	11.8	25.1	0.0211	0.282	1.89	
2004-09-03 max. log \mathcal{L}	7.15			0.0677			54.0			2.14			0.00561			Weak Homogeneous
2004-09-03 quantiles	6.97	7.18	7.41	0.0355	0.0590	0.0812	51.2	56.4	62.1	1.88	2.07	2.65	0.00382	0.00637	0.0122	
2004-10-07 max. log \mathcal{L}	4.55			1.53			73.5			4.64			0.054			Weak Homogeneous
2004-10-07 quantiles	4.47	4.55	4.62	1.53	1.53	1.60	70.0	73.2	75.3	4.62	4.69	4.96	0.0344	0.0626	0.101	
2006-12-09 max. log \mathcal{L}	3.65			5.26			35.5			5.64			9.41			Heterogeneous
2006-12-09 quantiles	3.25	3.58	3.99	5.24	5.28	5.36	29.7	37.2	44.1	5.51	5.64	6.25	2.60	4.63	9.11	
2009-10-08 max. log \mathcal{L}^*	6.23			10.4			35.7			186			26.1			Strong Aggregate
2009-10-08 quantiles*	6.15	6.24	6.35	9.18	10.0	12.5	30.3	34.4	37.7	183	188	194	24.7	25.8	27.2	
2010-07-06 max. log \mathcal{L}	5.77			0.218			79.7			11.9			0.984			Weak Homogeneous
2010-07-06 quantiles	5.76	6.05	6.26	0.232	0.304	0.399	77.0	85.2	89.7	7.54	8.27	11.2	0.349	0.667	1.23	
2010-12-25 max. log \mathcal{L}^*	7.93			3.06			28.3			50.3			3.11			Heterogeneous
2010-12-25 quantiles*	7.66	7.92	8.36	2.80	2.99	3.20	10.6	25.2	39.7	25.1	48.6	65.8	1.86	3.03	4.68	
2013-02-15 max. log \mathcal{L}	112			2.51			35.6			10.0			0.0374			Heterogeneous
2013-02-15 quantiles	111	113	119	2.18	2.51	2.52	34.5	49.5	91.4	7.61	9.63	14.3	0.0287	0.0686	0.534	
2013-04-30 max. log \mathcal{L}	7.83			4.56			86.1			9.15			0.254			Strong Homogeneous
2013-04-30 quantiles	7.41	7.71	7.96	4.45	4.55	4.56	77.0	83.8	89.3	8.63	9.39	10.2	0.201	0.273	0.549	
2016-02-06 max. log \mathcal{L}	5.35			1.36			31.7			3.59			0.0365			Heterogeneous
2016-02-06 quantiles	5.27	5.44	5.63	1.32	1.36	1.40	27.2	32.1	38.3	3.42	3.55	3.76	0.0251	0.0523	0.481	
2018-12-18 max. log \mathcal{L}^*	6.38			9.41			54.2			76.5			1.36			Strong Aggregate
2018-12-18 quantiles*	6.22	6.50	10.0	7.92	9.41	9.43	12.0	44.0	54.3	65.0	104	243	1.16	2.78	16.9	
2020-12-22 max. log \mathcal{L}	8.41			1.07			62.2			1.44			0.116			Weak Homogeneous
2020-12-22 quantiles	7.78	8.50	10.0	1.05	1.07	1.10	41.2	62.1	73.9	1.31	1.61	2.69	0.113	0.693	9.599	

Table 3. The maximum log-likelihood fit and nested sampling posterior quantiles for the physical parameters of 13 decameter impactors. Entries marked with an asterisk (*) have had their USG sensor-recorded light curves truncated due to contamination by reflected sunlight from the dust trail at low altitudes. The structural class of each object identified in Section 5.1 is also listed.

shall Islands fireball) fit using our procedure, while Figure 8b) shows the marginal 2D posterior distributions of dynamic pressure vs. mass released for each fragment and at peak dynamic pressure obtained using nested sampling. The fit light curves and marginal 2D posterior distributions of dynamic pressure vs. mass released for the other 12 decameter impactors are shown in Figures S1-S24 in Supporting Information S1. The cumulative mass released for each object as a function of dynamic pressure is shown in Figure 9.

From these results, we identify three broad classes of objects within the decameter impactor population. We also correlate the probable escape regions in the main-belt for decameter impactors with these strength classes to examine if there are any obvious links between their dynamical origins and material/structural properties.

5.1 Structural Properties

The only material strength classification of large meteoroids and small asteroids proposed to date is given by Borovička et al. (2020), which we adopt in this work and briefly summarize here.

In their proposed classification, the strongest objects are composed of Category A material which has tensile strength 20–40 MPa and represent compact, monolithic objects that can survive passage through the Earth’s atmosphere and be recovered as meteorites. Category B material has tensile strength 1–5 MPa and represents macroscopically cracked material weakened by asteroid collisions in space. Favorable entry condi-

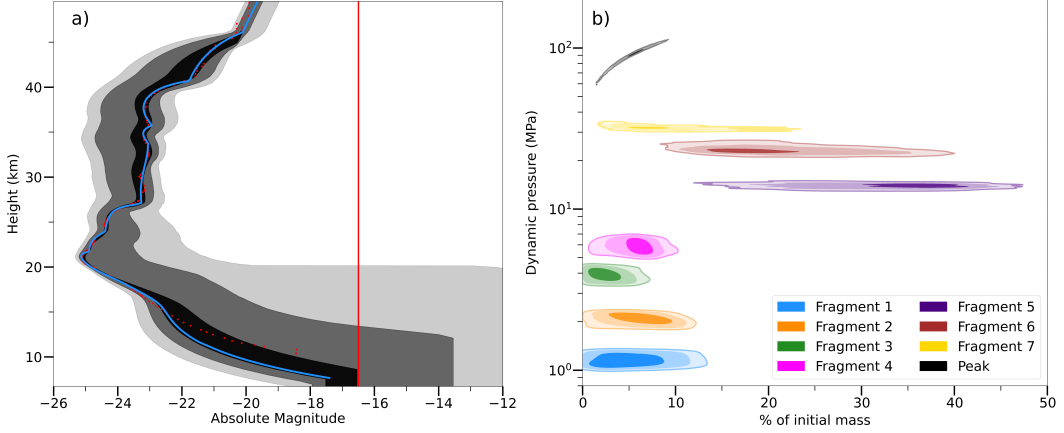


Figure 8. a): The observed light curve and corresponding model fit for the 1 February 1994 Marshall Islands fireball, similar to Figure 1a). b): The posterior distributions for dynamic pressure against mass released for each fragmentation point and mass remaining at peak dynamic pressure, similar to Figure 1b).

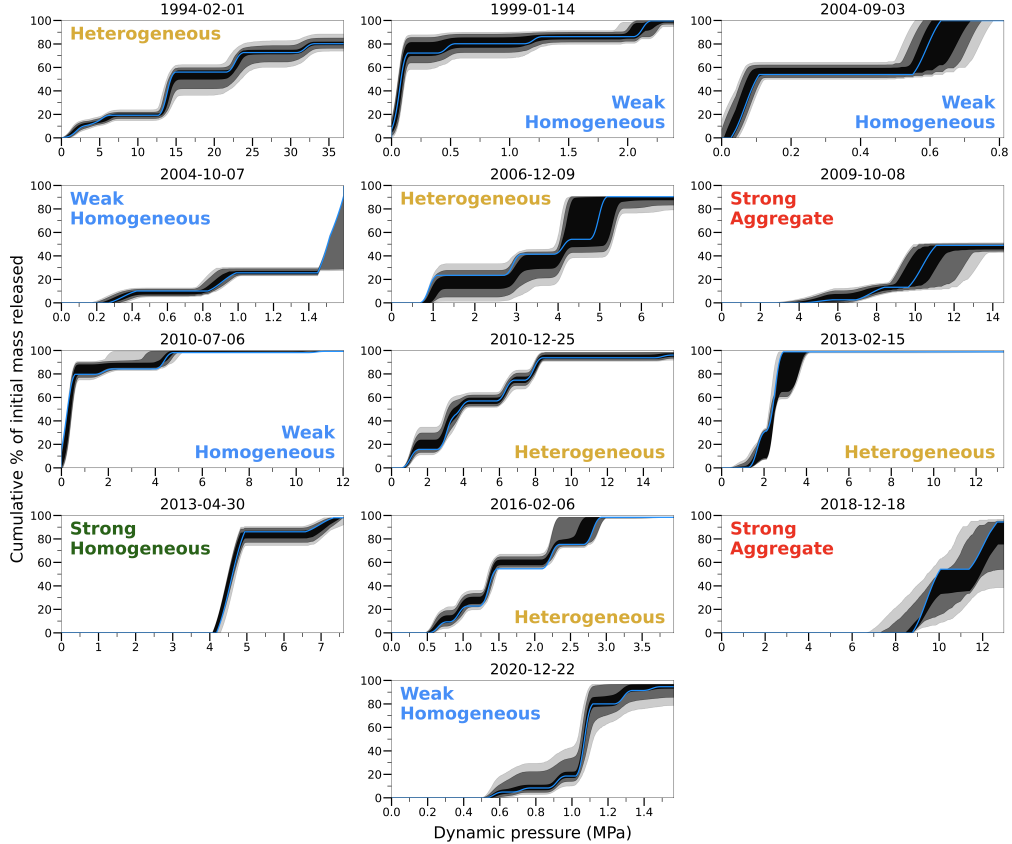


Figure 9. A staircase plot showing the cumulative mass released (expressed as a percentage of the initial mass) by 13 decameter-size impactors as a function of dynamic pressure, in MPa. Each object is identified by its UTC date (YYYY-MM-DD) of impact. The structural class of each object is also indicated. The black shaded regions illustrate the 1σ , 2σ and 3σ distributions of the cumulative mass released at a given dynamic pressure. The cumulative mass release corresponding to the maximum log-likelihood solution for each impactor is plotted in blue.

tions may allow meteorites to survive to the ground from these objects. Category C material has tensile strength 0.04–0.12 MPa and represents collisional debris that has been reassembled and cemented onto the surface of the meteoroid. This grade of material is quickly separated from the meteoroid during atmospheric entry and released at high altitudes. Finally, they propose the weakest material as “Category D” type. This material has virtually no tensile strength (~ 0 MPa) and represents rubble-pile asteroids loosely bound by gravity or van der Waals forces. This type of material fragments too quickly upon atmospheric entry to be detectable as part of meteoroid ablation and remains speculative (Borovička, 2015), though dedicated observations of fireballs early in flight have found formation of wake indicating grain release at very low dynamic pressures (~ 5 kPa; Shrbený et al., 2020).

From our analysis, we find that the decameter impactor population shows significant diversity cross-cutting these strength categories even for our small dataset. The clearest grouping consists of the 14 January 1999, 3 September 2004, 7 October 2004, 6 July 2010 and 22 December 2020 bolides. These are all globally weak objects where in all cases, most ($\gtrsim 80\%$) of the object’s initial mass was released at relatively low dynamic pressure ($\lesssim 1.5$ MPa) and only a small amount ($< 1\%$) of the object’s initial mass survived to peak dynamic pressure. We suggest that the October 2004 and December 2020 bolides are comprised of weak, heavily fractured category B material released mostly at the main fragmentation point. The January 1999, September 2004 and July 2010 bolides are even weaker objects comprised mostly of category C material, consisting of reassembled collisional debris cemented together with a global tensile strength of ~ 0.1 MPa, in addition to a small amount of slightly stronger category B material. We therefore suggest these five objects form a relatively distinct class comparable to the Romanian bolide, representing weak, structurally homogeneous (which we term weak homogeneous) bodies that completely disintegrate in the atmosphere and do not produce meteorites (Borovička et al., 2017).

The 30 April 2013 bolide displays similar structural homogeneity to the weak bolides but is significantly stronger overall, releasing $\sim 85\%$ of its initial mass in the main fragmentation at ~ 4.5 MPa. Based on the fragmentation behaviour, we suggest the April 2013 bolide is structurally similar to (though somewhat weaker than) the L5 chondrite Park Forest (Simon et al., 2004), which we estimate as having released $\sim 85\%$ of its mass at the ~ 6.3 MPa main burst and whose fit light curve is very similar in shape (compare Figure 3a) and Figure S17 in Supporting Information S1). It forms a class of its own which we term strong homogeneous.

In contrast, the 1 February 1994, 9 December 2006, 25 December 2010 and 6 February 2016 bolides display significant structural heterogeneity, characterized by multiple, extended fragmentation episodes. In all cases at least five major fragmentations were identified starting at ~ 1 MPa, and with no single fragment comprising more than $\sim 40\%$ of the object’s total mass. The maximum strength of these objects varies, with the last fragmentation at ~ 35 MPa, ~ 5.5 MPa, ~ 8 MPa, and ~ 3.5 MPa respectively. Based on the dynamic pressure range and numerous large fragmentations, we suggest that the latter three objects are composed almost entirely of category B material, with tensile strength ranging from 1–5 MPa. The February 1994 bolide stands out as an exceptionally strong object that likely contained a significant amount of extremely strong category A material or as suggested previously was perhaps made of iron (Nemtchinov, 1994). We therefore suggest these four bolides represent a class of structurally heterogeneous objects that incrementally fragment along cracks when the dynamic pressure reaches the tensile strength of that fragment, often with a small portion of the object (up to a few percent of the initial mass) surviving up to a high peak dynamic pressure. These strong inclusions may represent essentially intact “boulders” of high strength, similar to that found by Borovička, Spurný, et al. (2013) for the Chelyabinsk bolide whereby $\sim 1\%$ of the initial meteoroid mass was composed of relatively strong meter-sized “boulders”.

The 15 February 2013 Chelyabinsk bolide represents a special case as it is the only decameter impactor for which detailed ablation/fragmentation modeling has previously been conducted and we discuss it here separately. Analysis by Borovička, Spurný, et al. (2013) using the light curve of P. G. Brown et al. (2013) in conjunction with ground-based video footage and acoustic analysis suggests that the first major fragmentation occurred at a height of 45 km and dynamic pressure of ~ 0.7 MPa, followed by a series of 11 individual fragmentations between 40–30 km height and 1–5 MPa dynamic pressure in which most of the total mass was released. A tiny portion ($\sim 1\%$) penetrated much deeper into the atmosphere as a collection of large, strong fragments, surviving dynamic pressures of 10 – 20 MPa before fragmenting. At least one fragment impacted into Lake Chebarkul and was later recovered as a 570 kg meteorite. To simplify our model, we chose to approximate the series of 11 fragmentations between 40–30 km with three large fragmentation episodes as this produces a reasonable fit to the observed light curve. The light curve is the only data constraint we use here for consistency in our modeling approach with other USG bolides. However, based on the large number of fragmentations and dynamic pressure range identified by Borovička, Spurný, et al. (2013) using additional ground-based video data we suggest that Chelyabinsk is materially similar to our structurally heterogeneous object class (which we term simply heterogeneous as they span the spectrum from weak to strong) and composed mostly of category B material with a global strength of order 1 – 5 MPa.

The 8 October 2009 and 18 December 2018 fireballs are relatively unique objects that we discuss separately. Both are very energetic (30 – 50 kT TNT), occurred during daylight and based on their light curves remained mostly intact until the main fragmentation at 9 – 10 MPa. This is well above the maximum strength of cracked category B material (~ 5 MPa) yet much less than the tensile strength of pristine category A meteorites (~ 20 – 40 MPa).

We suggest that the peak dynamic pressure for these objects is significantly overestimated as light curves for these two objects have been truncated at low altitudes (due to likely persistent trail emission following the main airburst) but this has minimal effect on the inferred dynamic pressure at the main fragmentation and mass loss fraction up to the height of peak brightness. Despite the dimmer late persistent emission which makes it appear as though there was very low altitude ablation, most of the energy deposition occurs near the height of peak brightness where dust emission is less significant and hence the energies for these objects are likely not overestimated. Indeed, analysis by Silber et al. (2011) of worldwide infrasound from the 8 October 2009 fireball suggests a most likely energy of 50 kT TNT. More recently, Arrowsmith et al. (2021) analyzed infrasound from the 18 December 2018 bolide, finding an average period of 14.8 sec using select stations with high signal-to-noise ratio. We performed a similar analysis of signals from 15 infrasound stations and find a mean period of 16.3 sec. Using the multi-station average relation of Ens et al. (2012), these periods correspond to source energies of 35 and 49 kT TNT respectively, both of which are close to the USG-reported energy of 49 kT TNT.

These two bolides plausibly represent a separate, unique class of stronger objects whose structure is dominated by microcracks or microporosity rather than macroscopic fractures created by asteroid collisions alone. We term these objects strong aggregates.

5.2 Source Regions

We also analyze the origins of these decameter impactors from the main asteroid belt to see if any correlations exist with their structural properties. Chow and Brown (2025) used the NEO model of Granvik et al. (2018) to determine the probable source regions of the decameter impactors from their pre-impact orbits, generating 1000 Monte Carlo clones per object to estimate orbital uncertainties. The decameter impactor pop-

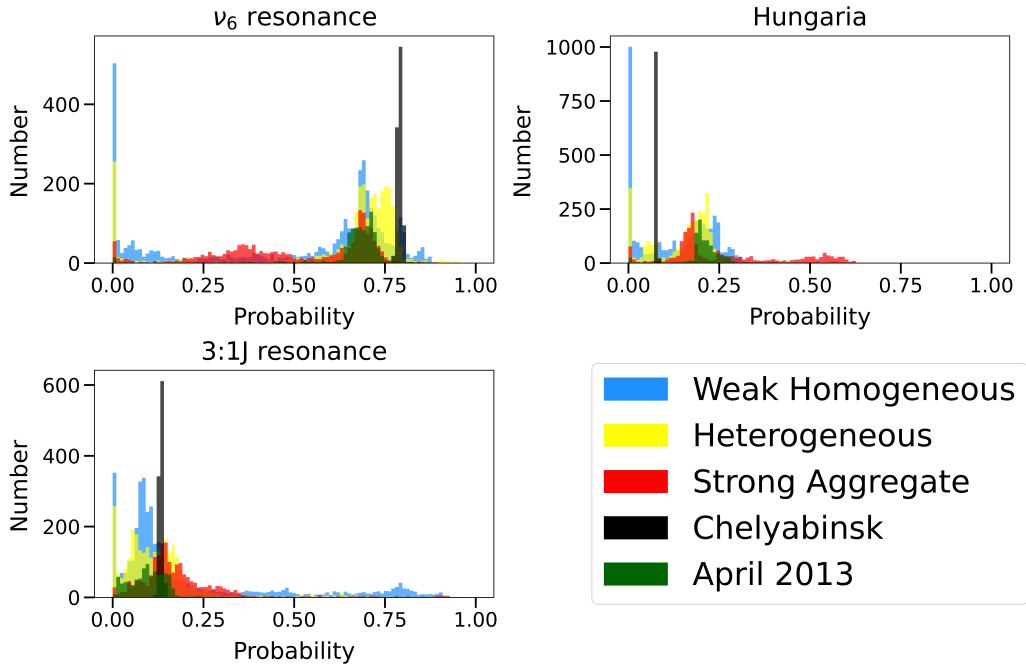


Figure 10. Histograms of source region probabilities for all USG sensor-detected decameter impactors and corresponding Monte Carlo clones for each of the three broad strength categories (weak homogeneous, heterogeneous, and strong aggregate) identified in the text, computed using the NEO model of Granvik et al. (2018). The Chelyabinsk (February 2013) and April 2013 bolides are plotted separately. Only the three primary source regions of decameter impactors (the ν_6 secular resonance, Hungaria family and 3:1 mean-motion resonance with Jupiter) identified by Chow and Brown (2025) are shown here, as the contributions of other source regions to the decameter impactor population are negligible.

ulation was found to originate from the ν_6 secular resonance with a probability of $\sim 70\%$, the Hungaria group with a probability of $\sim 20\%$ and the 3:1 Jupiter mean-motion resonance with a probability of $\sim 10\%$. No significant escape probabilities were found from the mid to outer main belt. Figure 10 shows the decameter impactor source region probabilities computed in Chow and Brown (2025) broken down by each of the broad strength classes (weak homogeneous, heterogeneous, and strong aggregate) identified in this work. The Chelyabinsk (February 2013) and April 2013 bolides are plotted separately: the former as its orbit (and therefore probable source region) is far better characterized than the other decameter impactors, and the latter as it is significantly stronger than the other homogeneous bodies.

To zeroth order, the distribution of source region probabilities for each of our strength classes is generally consistent with the population-level results found in Chow and Brown (2025), with no significant difference between expected source regions based on material strength. However, we note that our proposed classification and associated conclusions are tentative as they are limited by small-number statistics. As such, we do not strictly rule out a connection between dynamical origin and material strength for the decameter impactors, but merely conclude that there is no strong evidence for such a connection based on the currently limited number of detections.

6 Discussion

6.1 Uncertainties and Limitations in Analysis

Here we discuss sources of uncertainty as well as some of the choices made for our light curve modeling procedure and results of alternative methods that were explored. While we adopted fixed luminosity uncertainty in our modelling procedure, we also attempted to fit the light curves with intrinsic scatter/prediction error as a free parameter in the model to further improve our posterior estimates. This was done using a modified log-likelihood formalism \mathcal{L}' that adds a free intrinsic scatter term σ_{scat}^2 (parameterized as $\log\sigma_{\text{scat}}^2$ in the nested sampling) to the error, in quadrature with the observational uncertainty σ_i^2 , according to

$$\ln \mathcal{L}' (\Theta, \sigma_{\text{scat}}^2) = - \sum_{i=1}^N \left(\frac{(L_i - \bar{L}_i(\Theta))^2}{2(\sigma_i^2 + \sigma_{\text{scat}}^2)} + \ln \sqrt{2\pi(\sigma_i^2 + \sigma_{\text{scat}}^2)} \right). \quad (3)$$

In this case the first term of Equation 3 corresponds to the traditional reduced χ^2 , while the second term acts as an error term that effectively penalizes for large values of scatter. We tested both uniform and inverse-gamma priors (the latter being the conjugate prior of a Gaussian) for the scatter in the nested sampling, with bounds chosen so the prior encompasses the sample variance of the residuals for a manually-fit initial solution. However, in both cases, we found that the nested sampler often performed very poorly for many fireballs, becoming stuck in regions of parameter space that produced solutions completely incongruous with the observed light curves. This could be due to large differences in intensity throughout the duration of the light curves, often up to several orders of magnitude. We also explored fitting the USG light curves using the luminous efficiency model of Borovička et al. (2020) instead of a constant value based on the CNEOS-reported radiated and kinetic energies for each impactor. However, this produced initial masses that were several orders of magnitude too large for the validation cases, likely as a result of the USG sensor bandpasses being significantly different from ground-based bandpasses. As such, we chose to use a constant luminous efficiency derived from USG light curve comparisons to infrasound energies as reported in P. Brown et al. (2002) as it produced mass estimates generally consistent with the literature.

For the validation cases, we considered only the major fragmentation points identified by previous works where light curves were fit manually. This was done in order to facilitate direct comparison with previous studies and reduce the complexity of the nested sampling procedure, as each additional fragment significantly increases the dimensionality of the parameter space. While several models with varying numbers of fragments could in principle be fit to each light curve and rigorously compared using evidence-based metrics such as the Bayes factor (the ratio of evidences $\mathcal{Z}_1/\mathcal{Z}_2$ for two different models) or the Bayesian information criterion (BIC; Schwarz, 1978), we have foregone this approach as the USG light curve data is not precise enough for such a procedure to be robust. Instead, we merely note that for the validation cases, the posterior distributions for initial mass, dynamic pressure and mass released at main fragmentation inferred by our models under conservative, flat priors solely from the USG light curves are consistent with previous estimates using independent observations. The resulting fits qualitatively match the observed light curves well, particularly near peak brightness where most of the energy (and mass) is released.

For completeness, we also reanalyzed the light curves of all validation events using the reported meteorite density as the initial, pre-impact bulk density (excluding the Romania fireball as no meteorites were recovered) instead of the 1500 kg m^{-3} estimate of Chow and Brown (2025), with the idea that this represents an upper limit for the bulk density in these cases. The reported meteorite bulk densities for all validation events are summarized in Table 4. The only decameter impactor for which meteorites were recovered is Chelyabinsk, which was an LL5 chondrite with meteorite bulk density of ~ 3300

Meteorite	Classification	Bulk Density (kg m ⁻³)	Reference
Tagish Lake	C2-ungrouped	1670	Flynn et al. (2018)
Morávka	H5	3590	Flynn et al. (2018)
Park Forest	L5	3900	Flynn et al. (2018)
Košice	H5	3430	Flynn et al. (2018)
Romanian Fireball		no meteorites recovered	
Sarıçık	HED	2929	Unsalan et al. (2019)
Flensburg	C1-ungrouped	1984	Borovička et al. (2021)

Table 4. The classifications and weighted-average bulk densities of meteorites recovered from the seven validation fireball events considered in this work.

kg m⁻³ (O. P. Popova et al., 2013). We found that this reanalysis did not significantly change the inferred parameter posterior distributions for any of the validation events, a result consistent with previous studies where fireball light curves were manually fit (e.g. Borovička et al., 2019).

For the velocity uncertainties, we attempted to empirically ground USG velocity errors using a set of common USG sensor and ground-based fireball measurements, as described in Chow and Brown (2025). The majority of fireballs in this calibration dataset had speed estimates that agreed to within 2 km s⁻¹ between ground-based and USG values, though a small number had differences approaching 8 km s⁻¹. Given that these simultaneously ground-based and USG observed events were of lower energy and shorter duration than our larger decameter impactors, we expect our uncertainties to be lower. Taking a typical speed uncertainty of 2 km s⁻¹, this implies an uncertainty of $\sim 20\text{--}30\%$ in absolute dynamic pressure, though the relative difference in dynamic pressure between fragmentation points can be expected to be much less. The same calibration dataset yields a mean height difference for peak brightness between USG and ground-based measurements of 3 km (P. G. Brown & Borovička, 2023). This is less than half an atmospheric scale height and therefore the height uncertainties should produce less than a factor of two uncertainty in absolute dynamic pressure.

Finally, we note that as the sensitivity of the USG sensors is near magnitude -16.5 , the brightness in the earliest portion of flight is not recorded. Measurements in this early luminous phase often show that distinct fragmentation in the form of wake formation does occur at high altitudes under very low dynamic pressure (Shrbený et al., 2020). We are entirely insensitive to this phase of fireball flight other than to say that such high altitude mass loss does not appear to be globally significant for decameter impactors.

6.2 Physical Interpretation and Implications for Planetary Defence

It is commonly assumed that strength (and hence fragmentation behaviour) for meter-sized and larger meteoroids follows a Weibull-like power-law (e.g. O. Popova et al., 2011; Flynn et al., 2018). This power-law is grounded in observations of terrestrial rock fracturing which show that larger rocks are weaker than smaller rocks on average (Hartmann, 1969). In terms of the change in fragment strength with mass, this relationship follows (O. Popova et al., 2011)

$$\sigma = \sigma_s (M_s/M)^\alpha, \quad (4)$$

where σ is the strength of a fragment of mass M , σ_s is the strength of a smaller reference mass of mass M_s and α is a power-law coefficient relating the change in strength across mass scales. We note that while the tensile strength of individual fragments on average increases at smaller sizes, the Weibull distribution is an idealization; real fire-

balls display a wide variation in strength scaling depending on the object and the meteorite type. Nevertheless, understanding bounds for α is important for planetary defense, where broad statistical distributions are used prior to impact to bracket expected ground damage (e.g. Wheeler et al., 2017; Mathias et al., 2017; Wheeler et al., 2018). Past estimates of α have generally ranged from 0.1–0.5 (Svetsov et al., 1995; O. Popova et al., 2019) though recognition of the large range found in fireball data have led those focusing on impact effects related to planetary defense to broaden estimates to as much as 0.05–1 (Wheeler et al., 2017) when considering the effect on fireball energy deposition.

In Figure 11 we show the range of fragmentation strengths as a function of mass estimated for our decameter impactors. Here we adopt a 30 MPa tensile strength for a 0.01 kg fragment for consistency with previous work (O. Popova et al., 2011). We find a wide spread in the strength scaling parameter α , with the commonly adopted range of 0.1–0.5 well supported by our measurements to decameter sizes. For comparison, Wheeler et al. (2017) found that values of α between 0.1–0.3 were best able to replicate typical burst heights when estimating equivalent point-source burst altitudes. Fitting equation 4 to the observed data using least-squares optimization yields an empirical best-fit value of $\alpha \approx 0.12 \pm 0.011$, though most of the observed data deviates from a theoretical Weibull power law, as shown in Figure 11. Our goal here is merely to produce an empirical estimation of the strength and fragmentation behaviour of decameter-size objects, which previous planetary defense studies have identified as the most likely to cause ground damage in the near future (e.g. Boslough et al., 2015), for the first time. As such, we simply state that the majority of decameter impactors are fit well qualitatively for values of α ranging from ~ 0 –0.3.

An important new result from fragmentation measurements of decimeter- to meter-sized chondritic meteoroids by Borovička et al. (2020) was the first evidence for two distinct fragmentation stages. The first stage was found to consist of fragmentation releasing mass under dynamic pressures of 0.04–0.12 MPa. Borovička et al. (2020) interpret this phase as evidence for weakly cemented or aggregate fines (i.e. category C material) held together after having been potentially produced during impact on the original (larger) parent body. Of the 21 chondritic-like fireballs/meteorite-dropping bolides examined, this phase released 40% or more of the total mass in the majority of cases.

Few events studied by Borovička et al. (2020) showed significant fragmentation between 0.12 and 0.9 MPa – material bound at these strengths is surprisingly absent in chondritic-like fireballs. They noted that this second phase of fragmentation was found to last from 0.9–5 MPa and typically released less total mass than the first stage as well as occasionally being absent for some bolides. This phase was interpreted as being due to more competent rocky material weakened by collisional cracks (category B material), reducing their strength compared to meteorites found in the lab by an order of magnitude or more.

Similar to Borovička et al. (2020), we find here that the majority (10 of 13) of our decameter impactors begin fragmenting under dynamic pressures less than 1 MPa. As shown in Figure 12, there is also evidence for two stages of fragmentation (compare to Figure 6 of Borovička et al. (2020)): one with a peak in mass loss at ~ 0.04 –0.09 MPa and a later peak occurring near 1–4 MPa. In contrast to the smaller objects studied by Borovička et al. (2020), we find the second stage of fragmentation is where the majority of mass is released for decameter objects while comparatively little mass is released in the first stage. While our peaks are distinguishable and compare well with the stages identified by Borovička et al. (2020), our ranges of fragmentation are more spread out. We suggest this may be a consequence of the lower accuracy of the heights/light curves from USG data and the limited number of fragmentation points adopted in our modeling approach compared to the higher quality data and more detailed modeling employed by Borovička et al. (2020).

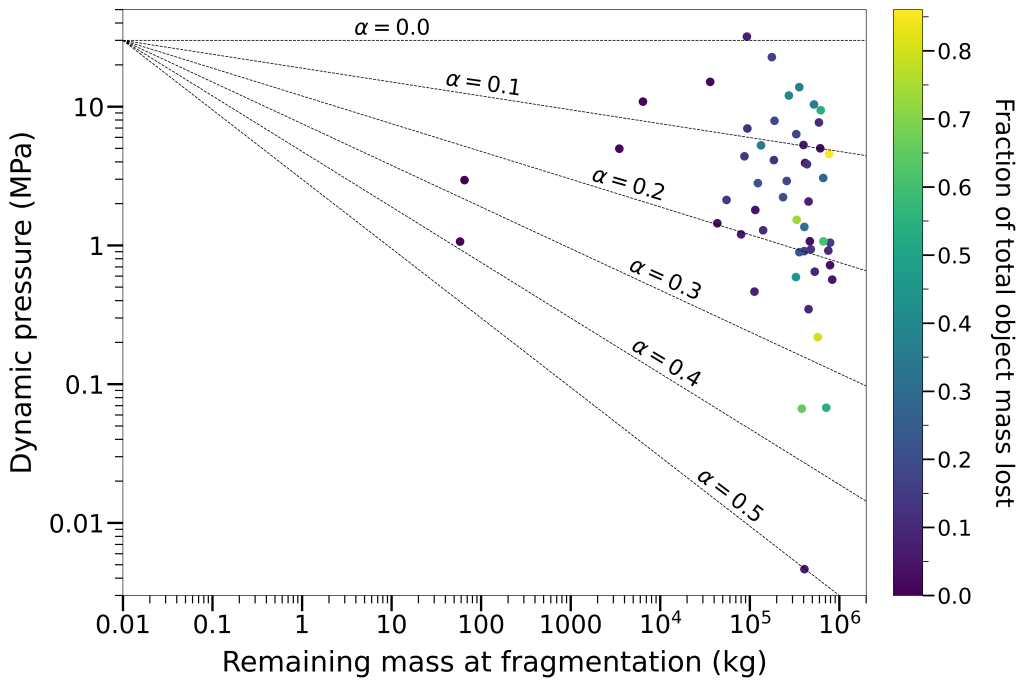


Figure 11. Dynamic pressure plotted against mass remaining at each fragmentation point for the maximum log-likelihood solutions of all 13 decameter impactors, with each point coloured by the fraction of total mass released. Assuming a tensile strength of 30 MPa for a 0.01 kg fragment, the black dashed lines show Weibull power-laws given by Equation 4 for values of the strength scaling parameter α ranging from 0.1 to 0.5. We find that values of α ranging from $\sim 0 - 0.3$ are appropriate to describe the fragmentation behaviour of decameter-size objects.

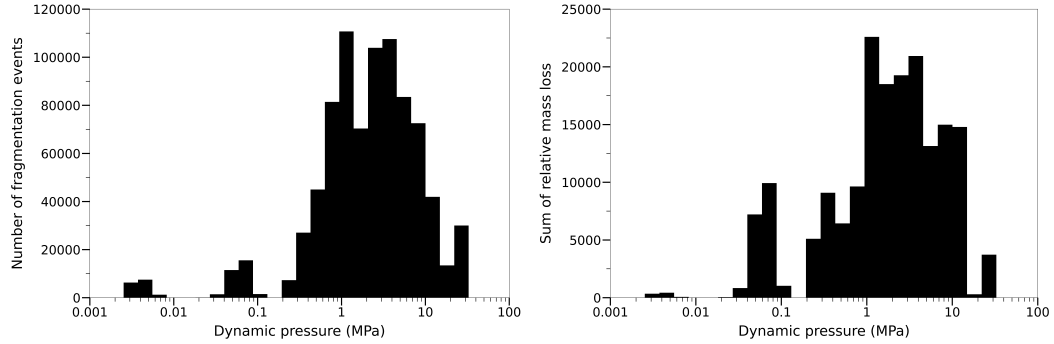


Figure 12. Histograms showing the distribution of dynamic pressures at major fragmentation points for all decameter impactors, using 15,000 samples drawn randomly from the nested sampling posteriors of each impactor. The left histogram is unweighted, while the right histogram shows each fragmentation event weighted by the relative mass loss.

We do not have sufficient information to determine whether our objects are chondrite-like material, carbonaceous chondrites or other meteorite analogs. We note that Borovička et al. (2020) explicitly mention the apparently different fragmentation behaviour of the fireball producing the Maribo carbonaceous chondrite fall (Borovička et al., 2019) and another EN-observed fireball for which similarly high-quality flight data was available. These objects seemingly do not show the two stage fragmentation behaviour, but rather have a large series of smaller fragmentations ranging from 0.25 – 4.3 MPa and 0.28 – 1.37 MPa respectively. These ranges are very similar to the 0.44–1.7 MPa tensile strength found for meter-size boulders on the asteroid Bennu (Ballouz et al., 2020) and the 0.2–0.28 MPa tensile strength estimate for a similar boulder on the asteroid Ryugu inferred from thermal measurements (Grott et al., 2019), yet less than the tensile strength for a variety of meteorites recovered on Earth (>10 MPa, except for C2-ungrouped, CI and CM chondrites; Ostrowski & Bryson, 2019) as well as recovered Ryugu samples of 1–8 mm size (Nakamura et al., 2022). As noted earlier, this reflects the overall increase in strength at smaller sizes. Among our decameter impactor sample, examination of Figure 9 shows that the 6 February 2016 and 22 December 2020 bolides most closely resemble the boulders, each having half a dozen discrete fragmentation events between ~ 0.5 –3 MPa.

That our decameter objects release more of their mass from cracked, rocky fragments may simply be a consequence of scale. The smaller decimeter- to meter-sized fireballs examined by Borovička et al. (2020) might be expected to release more cemented/weakly bound material from near-surface regions first, as these are proportionally a larger fraction of the volume for small objects. For our larger fireballs, the cemented material (if in an outer layer) may make up a much smaller total fraction of the object’s mass. We propose that at large (decameter) sizes, most impactors are composed of larger blocks riddled with cracks that fail at strengths between ~ 0.3 – 10 MPa.

7 Conclusions

In this work we have presented a new Bayesian inference method for robust inference of physical parameters of meteoroids. We fit a light curve to observations using the semi-empirical fragmentation model of Borovička, Tóth, et al. (2013) and estimate posterior distributions of the model parameters using dynamic nested sampling. We then validate our method by applying it to the newly released USG light curves of seven fireball events also observed separately by ground-based instruments. Finally, we apply this

method to the USG light curves of 13 decameter impactors identified in Chow and Brown (2025) to conduct the first population-level analysis of their material strength and physical structure. We summarize our major conclusions as follows:

1. The parameter values inferred by nested sampling when starting from wide, relatively uninformative priors and using only the USG sensor light curves are generally consistent with previous estimates determined by manual entry modelling of ground-based observations. The quantities most consistent with previous estimates are the dynamic pressure and mass released at the main fragmentation point. The initial mass is also generally consistent when taking into account systematic uncertainties in light curve calibration. The peak dynamic pressure can often be overestimated, especially in cases where an extended dust trail is present at low altitudes.
2. The decameter impactor population is structurally diverse within even the small number of known impactors. We identify the following three broad structurally distinct classes, based on the material strength classification proposed by Borovička et al. (2020).
 - (a) *Homogeneous meteoroids*. This group consists mainly of weak homogeneous objects such as the 14 January 1999, 3 September 2004, 7 October 2004, 6 July 2010 and 22 December 2020 fireballs. Most ($> 80\%$) of the object's mass is released below 1.5 MPa, often in just one or two large fragments, with less than 1% of the mass surviving to peak dynamic pressure. These objects are comprised of weak category B and some category C material. The 30 April 2013 bolide stands out in this broad group as noticeably stronger overall and might be better categorized as a strong homogeneous meteoroid.
 - (b) *Heterogeneous meteoroids*. This group consists of the 1 February 1994, 9 December 2006, 25 December 2010, 15 February 2013 and 6 February 2016 fireballs. The object undergoes numerous large fragmentations starting at ~ 1 MPa, with no single fragment making up more than $\sim 40\%$ of the object's initial mass. These objects are comprised of category B material, and in the case of the 1 February 1994 fireball a significant amount of category A material as well.
 - (c) *Globally strong meteoroids - Strong Aggregates*. This group consists of the 8 October 2009 and 18 December 2018 fireballs. Most ($> 80\%$) of the object's mass is released at the main fragmentation at 9–10 MPa. These bodies could possibly represent a unique class of objects whose global strength is between that of category B and A material, whose structure is primarily dominated by microporosity rather than large cracks.

We do not find any significant difference in the global strength of most decameter impactors compared to the smaller meteoroids examined by Borovička et al. (2020) and earlier by O. Popova et al. (2011). This is consistent with the notion that from centimeter-decameter sizes the strength of meteoroids is determined mainly by their unique collisional history as opposed to intrinsic material properties.

3. The probable source regions of each of the classes of decameter impactors identified above qualitatively match those of the population as a whole found by Chow and Brown (2025), with $\sim 70\%$ of objects coming from the ν_6 secular resonance, $\sim 20\%$ from the Hungaria family and $\sim 10\%$ from the 3:1 mean-motion resonance with Jupiter. There is no evidence for any link between the physical structure/material strength of decameter impactors and their dynamical origin.
4. We identify two distinct fragmentation phases for the decameter impactor population in which most mass is lost, with the first phase occurring at ~ 0.04 – 0.09 MPa and the second phase at ~ 1 – 4 MPa. This two-stage model of fragmentation and the corresponding dynamic pressures are very similar to those found by Borovička et al. (2020) for decimeter- to meter-size fireballs. However, while the first phase (representing category C material) dominates mass loss for meter-

size objects, we find that the second phase (representing category B material) is instead dominant for larger decameter-size objects.

5. The main implication of our strength study of decameter-size bolides is in the fragmentation parameters to be used in planetary defense models for similarly sized impactors. In particular, when rock strengths are modelled using a Weibull power law, the main mass release stage of such large impactors is best captured for values of the strength scaling parameter α between $\sim 0 - 0.3$. Moreover, ensuring the main fragmentation stage resides between $\sim 1 - 10$ MPa best captures the observed fragmentation process for decameter impactors.

The nested sampling method represents a powerful tool to estimate the physical properties of any meteoroid with an observed light curve, and can naturally be extended to fit for meteoroid dynamics as well when such measurements are available. We anticipate future applications of this method to other fireball light curves (including the hundreds of meter-size objects detected by USG sensors) in order to better understand the physical properties of meteoroids.

Conflict of Interest

The authors declare there are no conflicts of interest for this manuscript.

Open Research Section

All USG sensor fireball data, including light curves, are publicly available on the CNEOS website at <https://cneos.jpl.nasa.gov/fireballs/>. The semi-empirical model of Borovička, Tóth, et al. (2013) is implemented using the `MetSim` software (Vida et al., 2023). The dynamic nested sampling was conducted with the `dynesty` software package (Speagle, 2020; Koposov et al., 2024) in Python.

Acknowledgments

We sincerely thank the anonymous reviewers for providing feedback on an earlier version of this manuscript and Josh Speagle for providing many helpful discussions about `dynesty`. Funding for this work was provided in part by the Meteoroid Environment Office of NASA through co-operative agreement 80NSSC24M0060, the Natural Sciences and Engineering Research Council of Canada and the Canada Research Chairs program.

References

Arrowsmith, S., Negruaru, P., & Johnson, G. (2021, October). Bolide En-
ergetics and Infrasound Propagation: Exploring the 18 December 2018
Bering Sea Event to Identify Limitations of Empirical and Numerical Mod-
els. *The Seismic Record*, 1(3), 164–171. Retrieved 2025-06-10, from
<https://pubs.geoscienceworld.org/tsr/article/1/3/164/610370/Bolide-Energetics-and-Infrasound-Propagation> doi: 10.1785/0320210034

Ballouz, R.-L., Walsh, K. J., Barnouin, O. S., DellaGiustina, D. N., Asad, M. A.,
Jawin, E. R., ... Lauretta, D. S. (2020, November). Bennu's near-Earth
lifetime of 1.75 million years inferred from craters on its boulders. *Nature*,
587(7833), 205–209. Retrieved 2025-06-10, from <https://www.nature.com/articles/s41586-020-2846-z> (Publisher: Nature Publishing Group) doi:
10.1038/s41586-020-2846-z

Bischoff, A., Alexander, C. M. O., Barrat, J.-A., Burkhardt, C., Busemann, H.,
Degering, D., ... Wölfer, E. (2021, January). The old, unique C1 chondrite
Flensburg – Insight into the first processes of aqueous alteration, brecciation,
and the diversity of water-bearing parent bodies and lithologies. *Geochimica*

et *Cosmochimica Acta*, 293, 142–186. Retrieved 2025-04-09, from <https://www.sciencedirect.com/science/article/pii/S0016703720306463> doi: 10.1016/j.gca.2020.10.014

Bland, P. A., & Artemieva, N. A. (2006). The rate of small impacts on Earth. *Meteoritics & Planetary Science*, 41(4), 607–631. Retrieved 2024-12-26, from <https://onlinelibrary.wiley.com/doi/abs/10.1111/j.1945-5100.2006.tb00485.x> (eprint: <https://onlinelibrary.wiley.com/doi/pdf/10.1111/j.1945-5100.2006.tb00485.x>) doi: 10.1111/j.1945-5100.2006.tb00485.x

Borovicka, J., & Kalenda, P. (2003, July). The Morávka meteorite fall: 4 Meteoroid dynamics and fragmentation in the atmosphere. *Meteoritics and Planetary Science*, 38, 1023–1043. Retrieved 2025-04-11, from <https://ui.adsabs.harvard.edu/abs/2003M&PS...38.1023B> (ADS Bibcode: 2003M&PS...38.1023B) doi: 10.1111/j.1945-5100.2003.tb00296.x

Borovicka, J., Spurný, P., Kalenda, P., & Tagliaferri, E. (2003, July). The Morávka meteorite fall: 1 Description of the events and determination of the fireball trajectory and orbit from video records. *Meteoritics and Planetary Science*, 38, 975–987. Retrieved 2025-04-11, from <https://ui.adsabs.harvard.edu/abs/2003M&PS...38..975B> (ADS Bibcode: 2003M&PS...38..975B) doi: 10.1111/j.1945-5100.2003.tb00293.x

Borovicka, J., Weber, H. W., Jopek, T., Jakeš, P., Randa, Z., Brown, P. G., ... Brandstätter, F. (2003, July). The Morávka meteorite fall: 3 Meteoroid initial size, history, structure, and composition. *Meteoritics and Planetary Science*, 38, 1005–1021. Retrieved 2025-04-11, from <https://ui.adsabs.harvard.edu/abs/2003M&PS...38.1005B> (ADS Bibcode: 2003M&PS...38.1005B) doi: 10.1111/j.1945-5100.2003.tb00295.x

Borovička, J. (2015, August). Are some meteoroids rubble piles? *Proceedings of the International Astronomical Union*, 10(S318), 80–85. Retrieved from https://www.cambridge.org/core/product/identifier/S174392131500873X/type/journal_article doi: 10.1017/S174392131500873X

Borovička, J., Bettonvil, F., Baumgarten, G., Strunk, J., Hankey, M., Spurný, P., & Heinlein, D. (2021). Trajectory and orbit of the unique carbonaceous meteorite Flensburg. *Meteoritics & Planetary Science*, 56(3), 425–439. Retrieved 2025-02-26, from <https://onlinelibrary.wiley.com/doi/abs/10.1111/maps.13628> (eprint: <https://onlinelibrary.wiley.com/doi/pdf/10.1111/maps.13628>) doi: 10.1111/maps.13628

Borovička, J., Popova, O., & Spurný, P. (2019). The Maribo CM2 meteorite fall—Survival of weak material at high entry speed. *Meteoritics & Planetary Science*, 54(5), 1024–1041. Retrieved 2025-04-10, from <https://onlinelibrary.wiley.com/doi/abs/10.1111/maps.13259> (eprint: <https://onlinelibrary.wiley.com/doi/pdf/10.1111/maps.13259>) doi: 10.1111/maps.13259

Borovička, J., Spurný, P., Brown, P., Wiegert, P., Kalenda, P., Clark, D., & Shrbený, L. (2013, November). The trajectory, structure and origin of the Chelyabinsk asteroidal impactor. *Nature*, 503(7475), 235–237. Retrieved 2024-06-24, from <https://www.nature.com/articles/nature12671> doi: 10.1038/nature12671

Borovička, J., Spurný, P., Grigore, V. I., & Svoreň, J. (2017, September). The January 7, 2015, superbolide over Romania and structural diversity of meter-sized asteroids. *Planetary and Space Science*, 143, 147–158. Retrieved 2025-04-09, from <https://www.sciencedirect.com/science/article/pii/S0032063316303063> doi: 10.1016/j.pss.2017.02.006

Borovička, J., Spurný, P., & Shrbený, L. (2020, June). Two Strengths of Ordinary Chondritic Meteoroids as Derived from Their Atmospheric Fragmentation Modeling. *The Astronomical Journal*, 160(1), 42. Retrieved 2025-02-12, from

<https://dx.doi.org/10.3847/1538-3881/ab9608> (Publisher: The American Astronomical Society) doi: 10.3847/1538-3881/ab9608

Borovička, J., Tóth, J., Igaz, A., Spurný, P., Kalenda, P., Haloda, J., ... Husárik, M. (2013). The Košice meteorite fall: Atmospheric trajectory, fragmentation, and orbit. *Meteoritics & Planetary Science*, 48(10), 1757–1779. Retrieved 2025-02-26, from <https://onlinelibrary.wiley.com/doi/abs/10.1111/maps.12078> (.eprint: <https://onlinelibrary.wiley.com/doi/pdf/10.1111/maps.12078>) doi: 10.1111/maps.12078

Boslough, M., Brown, P., & Harris, A. (2015, March). Updated population and risk assessment for airbursts from near-earth objects (NEOs). In *2015 IEEE Aerospace Conference* (pp. 1–12). Retrieved 2024-06-24, from <https://ieeexplore.ieee.org/document/7119288> (ISSN: 1095-323X) doi: 10.1109/AERO.2015.7119288

Brown, P., Pack, D., Edwards, W. N., Revelle, D. O., Yoo, B. B., Spalding, R. E., & Tagliaferri, E. (2004). The orbit, atmospheric dynamics, and initial mass of the Park Forest meteorite. *Meteoritics & Planetary Science*, 39(11), 1781–1796. Retrieved 2025-04-11, from <https://onlinelibrary.wiley.com/doi/abs/10.1111/j.1945-5100.2004.tb00075.x> (.eprint: <https://onlinelibrary.wiley.com/doi/pdf/10.1111/j.1945-5100.2004.tb00075.x>) doi: 10.1111/j.1945-5100.2004.tb00075.x

Brown, P., Spalding, R. E., ReVelle, D. O., Tagliaferri, E., & Worden, S. P. (2002, November). The flux of small near-Earth objects colliding with the Earth. *Nature*, 420(6913), 294–296. Retrieved 2024-09-26, from <https://www.nature.com/articles/nature01238> (Publisher: Nature Publishing Group) doi: 10.1038/nature01238

Brown, P. G., Assink, J. D., Astiz, L., Blaauw, R., Boslough, M. B., Borovička, J., ... Krzeminski, Z. (2013, November). A 500-kiloton airburst over Chelyabinsk and an enhanced hazard from small impactors. *Nature*, 503, 238–241. Retrieved from <http://www.nature.com/doifinder/10.1038/nature12741> doi: 10.1038/nature12741

Brown, P. G., & Borovička, J. (2023, August). On the Proposed Interstellar Origin of the USG 20140108 Fireball. *The Astrophysical Journal*, 953(2), 167. Retrieved 2024-06-19, from <https://dx.doi.org/10.3847/1538-4357/ace421> doi: 10.3847/1538-4357/ace421

Brown, P. G., ReVelle, D. O., Tagliaferri, E., & Hildebrand, A. R. (2002). An entry model for the Tagish Lake fireball using seismic, satellite and infrasound records. *Meteoritics & Planetary Science*, 37(5), 661–675. Retrieved 2025-04-11, from <https://onlinelibrary.wiley.com/doi/abs/10.1111/j.1945-5100.2002.tb00846.x> (.eprint: <https://onlinelibrary.wiley.com/doi/pdf/10.1111/j.1945-5100.2002.tb00846.x>) doi: 10.1111/j.1945-5100.2002.tb00846.x

Ceplecha, Z., & Revelle, D. O. (2005, January). Fragmentation model of meteoroid motion, mass loss, and radiation in the atmosphere. *Meteoritics and Planetary Science*, 40, 35. Retrieved 2025-04-10, from <https://ui.adsabs.harvard.edu/abs/2005M&PS...40...35C> (ADS Bibcode: 2005M&PS...40...35C) doi: 10.1111/j.1945-5100.2005.tb00363.x

Ceplecha, Z., Spurný, P., Borovicka, J., & Keclíkova, J. (1993, November). Atmospheric fragmentation of meteoroids. *Astronomy and Astrophysics*, 279, 615–626. Retrieved 2025-04-20, from <https://ui.adsabs.harvard.edu/abs/1993A&A...279..615C> (ADS Bibcode: 1993A&A...279..615C)

Chow, I., & Brown, P. G. (2025, March). Decameter-sized Earth impactors – I: Orbital properties. *Icarus*, 429, 116444. Retrieved 2024-12-27, from <https://www.sciencedirect.com/science/article/pii/S0019103524005049> doi: 10.1016/j.icarus.2024.116444

Clark, D. L., Wiegert, P. A., Brown, P. G., Vida, D., Heinze, A., & Denneau, L. (2023, June). Preatmospheric Detection of a Meter-sized Earth Impactor. *The Planetary Science Journal*, 4(6), 103. Retrieved 2025-03-24, from <https://iopscience.iop.org/article/10.3847/PSJ/acc9b1/meta> (Publisher: IOP Publishing) doi: 10.3847/PSJ/acc9b1

Devillepoix, H. A. R., Bland, P. A., Sansom, E. K., Towner, M. C., Cupák, M., Howie, R., ... Cox, M. A. (2019, March). Observation of metre-scale impactors by the Desert Fireball Network. *Monthly Notices of the Royal Astronomical Society*, 483(4), 5166–5178. Retrieved from <http://arxiv.org/abs/1808.09195> doi: 10.1093/mnras/sty3442

Egal, A., Vida, D., Colas, F., Zanda, B., Bouley, S., Steinhausser, A., ... Jenniskens, P. (2025, September). Catastrophic disruption of asteroid 2023 CX1 and implications for planetary defence. *Nature Astronomy*, 1–14. Retrieved 2025-11-01, from <https://www.nature.com/articles/s41550-025-02659-8> (Publisher: Nature Publishing Group) doi: 10.1038/s41550-025-02659-8

Ens, T., Brown, P. G., Edwards, W. N., & Silber, E. (2012, May). Infra-sound production by bolides: A global statistical study. *Journal of Atmospheric and Solar-Terrestrial Physics*, 80, 208–229. Retrieved from <http://linkinghub.elsevier.com/retrieve/pii/S1364682612000326> (Publisher: Elsevier) doi: 10.1016/j.jastp.2012.01.018

Fisher, R. (1922, January). On the mathematical foundations of theoretical statistics. *Philosophical Transactions of the Royal Society of London. Series A, Containing Papers of a Mathematical or Physical Character*, 222(594-604), 309–368. Retrieved 2025-04-15, from <https://royalsocietypublishing.org/doi/10.1098/rsta.1922.0009> doi: 10.1098/rsta.1922.0009

Flynn, G. J., Consolmagno, G. J., Brown, P., & Macke, R. J. (2018, September). Physical properties of the stone meteorites: Implications for the properties of their parent bodies. *Geochemistry*, 78(3), 269–298. Retrieved 2025-05-09, from <https://www.sciencedirect.com/science/article/pii/S0009281916302860> doi: 10.1016/j.chemer.2017.04.002

Foreman-Mackey, D., Hogg, D. W., Lang, D., & Goodman, J. (2013, February). emcee: The MCMC Hammer. *Publications of the Astronomical Society of the Pacific*, 125(925), 306. Retrieved 2024-06-13, from <https://iopscience.iop.org/article/10.1086/670067/meta> (Publisher: IOP Publishing) doi: 10.1086/670067

Geng, S., Zhou, B., & Li, M. (2023, February). Near-Earth object 2022 EB5: From atmospheric entry to physical properties and orbit. *Astronomy & Astrophysics*, 670, A27. Retrieved 2025-12-22, from <https://www.aanda.org/articles/aa/abs/2023/02/aa44084-22/aa44084-22.html> (Publisher: EDP Sciences) doi: 10.1051/0004-6361/202244084

Gi, N., & Brown, P. (2017, September). Refinement of bolide characteristics from infrasound measurements. *Planetary and Space Science*, 143, 169–181. Retrieved 2024-08-02, from <https://www.sciencedirect.com/science/article/pii/S0032063316302604> doi: 10.1016/j.pss.2017.04.021

Gianotto, F., Carbognani, A., Fenucci, M., Devogèle, M., Ramirez-Moreta, P., Micheli, M., ... Rudawska, R. (2025, June). The fall of asteroid 2024 XA1<math><msub is="true"><mrow is="true"></mrow><mrow is="true"><mn is="true">1</mn></mrow></msub></math> and the location of possible meteorites. *Icarus*, 433, 116511. Retrieved 2025-11-05, from <https://www.sciencedirect.com/science/article/pii/S0019103525000582> doi: 10.1016/j.icarus.2025.116511

Goodman, J., & Weare, J. (2010, January). Ensemble samplers with affine invariance. *Communications in Applied Mathematics and Computational Science*, 5(1), 65–80. Retrieved 2024-09-24, from <https://msp.org/camcos/2010/5-1/p04.xhtml> (Publisher: Mathematical Sciences Publishers) doi:

10.2140/camcos.2010.5.65

Granvik, M., Morbidelli, A., Jedicke, R., Bolin, B., Bottke, W., Beshore, E., ... Michel, P. (2018, September). Debiased orbit and absolute-magnitude distributions for near-Earth objects. *Icarus*, 312, 181–207. Retrieved from <https://linkinghub.elsevier.com/retrieve/pii/S0019103517307017> doi: 10.1016/j.icarus.2018.04.018

Grott, M., Knollenberg, J., Hamm, M., Ogawa, K., Jaumann, R., Otto, K. A., ... Moussi-Soffys, A. (2019, November). Low thermal conductivity boulder with high porosity identified on C-type asteroid (162173) Ryugu. *Nature Astronomy*, 3(11), 971–976. Retrieved 2025-06-10, from <https://www.nature.com/articles/s41550-019-0832-x> (Publisher: Nature Publishing Group) doi: 10.1038/s41550-019-0832-x

Handley, W. J., Hobson, M. P., & Lasenby, A. N. (2015a, June). polychord: nested sampling for cosmology. *Monthly Notices of the Royal Astronomical Society: Letters*, 450(1), L61–L65. Retrieved 2025-04-16, from <https://doi.org/10.1093/mnrasl/slv047> doi: 10.1093/mnrasl/slv047

Handley, W. J., Hobson, M. P., & Lasenby, A. N. (2015b, November). polychord: next-generation nested sampling. *Monthly Notices of the Royal Astronomical Society*, 453(4), 4384–4398. Retrieved 2025-04-16, from <https://doi.org/10.1093/mnras/stv1911> doi: 10.1093/mnras/stv1911

Hankey, M., Perlerin, V., & Meisel, D. (2020, October). The all-sky-6 and the Video Meteor Archive system of the AMS Ltd. *Planetary and Space Science*, 190, 105005. Retrieved 2025-04-09, from <https://www.sciencedirect.com/science/article/pii/S0032063319304805> doi: 10.1016/j.pss.2020.105005

Hartmann, W. K. (1969, March). Terrestrial, lunar, and interplanetary rock fragmentation. *Icarus*, 10(2), 201–213. Retrieved 2025-06-10, from <https://www.sciencedirect.com/science/article/pii/0019103569900220> doi: 10.1016/0019-1035(69)90022-0

Henych, T., Borovička, J., & Spurný, P. (2023, March). Semi-automatic meteoroid fragmentation modeling using genetic algorithms. *Astronomy & Astrophysics*, 671, A23. Retrieved 2024-08-08, from <https://www.aanda.org/articles/aa/abs/2023/03/aa45023-22/aa45023-22.html> (Publisher: EDP Sciences) doi: 10.1051/0004-6361/202245023

Higson, E., Handley, W., Hobson, M., & Lasenby, A. (2019, September). Dynamic nested sampling: an improved algorithm for parameter estimation and evidence calculation. *Statistics and Computing*, 29(5), 891–913. Retrieved 2025-03-24, from <https://doi.org/10.1007/s11222-018-9844-0> doi: 10.1007/s11222-018-9844-0

Hildebrand, A. R., McCausland, P. J. A., Brown, P. G., Longstaffe, F. J., Russell, S. D. J., Tagliaferri, E., ... Mazur, M. J. (2006, March). The fall and recovery of the Tagish Lake meteorite. *Meteoritics and Planetary Science*, 41, 407–431. Retrieved 2025-04-11, from <https://ui.adsabs.harvard.edu/abs/2006M&PS...41..407H> (ADS Bibcode: 2006M&PS...41..407H) doi: 10.1111/j.1945-5100.2006.tb00471.x

Ingebretsen, C., Bolin, B. T., Jedicke, R., Vereš, P., Chen, C. H., Lisse, C. M., ... Townsend, A. J. (2025, September). Apache Point Rapid Response Characterization of Primitive Imminent Impactor 2024 RW1. *The Astronomical Journal*, 170(4), 237. Retrieved 2025-11-01, from <https://doi.org/10.3847/1538-3881/adfb63> (Publisher: The American Astronomical Society) doi: 10.3847/1538-3881/adfb63

Ivezić, Ž., Kahn, S. M., Tyson, J. A., Abel, B., Acosta, E., Allsman, R., ... Zhan, H. (2019, March). LSST: From Science Drivers to Reference Design and Anticipated Data Products. *The Astrophysical Journal*, 873(2), 111. Retrieved 2024-09-23, from <https://dx.doi.org/10.3847/1538-4357/ab042c> (Publisher: The American Astronomical Society) doi: 10.3847/1538-4357/ab042c

Jenniskens, P., Albers, J., Tillier, C. E., Edgington, S. F., Longenbaugh, R. S., Goodman, S. J., ... Stern, E. (2018). Detection of meteoroid impacts by the Geostationary Lightning Mapper on the GOES-16 satellite. *Meteoritics & Planetary Science*, 53(12), 2445–2469. Retrieved 2025-04-25, from <https://onlinelibrary.wiley.com/doi/abs/10.1111/maps.13137> (_eprint: <https://onlinelibrary.wiley.com/doi/pdf/10.1111/maps.13137>) doi: 10.1111/maps.13137

Jenniskens, P., Gabadirwe, M., Yin, Q.-Z., Proyer, A., Moses, O., Kohout, T., ... Botepe, K. (2021). The impact and recovery of asteroid 2018 LA. *Meteoritics & Planetary Science*, 56(4), 844–893. Retrieved 2024-06-23, from <https://onlinelibrary.wiley.com/doi/abs/10.1111/maps.13653> (_eprint: <https://onlinelibrary.wiley.com/doi/pdf/10.1111/maps.13653>) doi: 10.1111/maps.13653

Jenniskens, P., Shaddad, M. H., Numan, D., Elsir, S., Kudoda, A. M., Zolensky, M. E., ... Worden, S. P. (2009, March). The impact and recovery of asteroid 2008 TC3. *Nature*, 458(7237), 485–488. Retrieved 2024-06-23, from <https://www.nature.com/articles/nature07920> (Publisher: Nature Publishing Group) doi: 10.1038/nature07920

Kareta, T., Vida, D., Micheli, M., Moskovitz, N., Wiegert, P., Brown, P. G., ... Farnocchia, D. (2024, November). Telescope-to-Fireball Characterization of Earth Impactor 2022 WJ1. *The Planetary Science Journal*, 5(11), 253. Retrieved 2025-03-24, from <https://iopscience.iop.org/article/10.3847/PSJ/ad8b22/meta> (Publisher: IOP Publishing) doi: 10.3847/PSJ/ad8b22

Koposov, S., Speagle, J., Barbary, K., Ashton, G., Bennett, E., Buchner, J., ... Goldstein, D. (2024, June). *joshspeagle/dynesty: v2.1.4*. Zenodo. Retrieved 2025-03-24, from <https://zenodo.org/doi/10.5281/zenodo.12537467> doi: 10.5281/ZENODO.12537467

Kurlander, J. A., Bernardinelli, P. H., Schwamb, M. E., Jurić, M., Murtagh, J., Chandler, C. O., ... Buchanan, L. E. (2025, July). Predictions of the LSST Solar System Yield: Near-Earth Objects, Main Belt Asteroids, Jupiter Trojans, and Trans-Neptunian Objects. *The Astronomical Journal*, 170(2), 99. Retrieved 2025-10-29, from <https://doi.org/10.3847/1538-3881/add685> (Publisher: The American Astronomical Society) doi: 10.3847/1538-3881/add685

Mainzer, A. K., Masiero, J. R., Abell, P. A., Bauer, J. M., Bottke, W., Buratti, B. J., ... Team, N. S. M. (2023, December). The Near-Earth Object Surveyor Mission. *The Planetary Science Journal*, 4(12), 224. Retrieved 2025-12-22, from <https://iopscience.iop.org/article/10.3847/PSJ/ad0468> (Publisher: IOP Publishing) doi: 10.3847/PSJ/ad0468

Mathias, D. L., Wheeler, L. F., & Dotson, J. L. (2017, June). A probabilistic asteroid impact risk model: assessment of sub-300 m impacts. *Icarus*, 289, 106–119. Retrieved 2025-06-10, from <https://www.sciencedirect.com/science/article/pii/S0019103516307126> doi: 10.1016/j.icarus.2017.02.009

McFadden, L., Brown, P. G., & Vida, D. (2024, November). A comparison of fireball luminous efficiency models using acoustic records. *Icarus*, 422, 116250. Retrieved 2024-12-23, from <https://www.sciencedirect.com/science/article/pii/S0019103524003105> doi: 10.1016/j.icarus.2024.116250

McKinney, E. D., Frazier, R., Pratt, J., Larsen, M., Nelson, P., & Gunther, H. (2025, March). ADVANCEMENTS IN NEAR REAL-TIME BOLIDE DETECTION: CONTINUUM CALIBRATION, ALTITUDE ESTIMATION, AND VELOCITY APPROXIMATION USING NOAA GOES GLM DATA. In *56th Annual Lunar and Planetary Science Conference* (p. 1236). The Woodlands, TX: LPI. Retrieved from <https://www.hou.usra.edu/meetings/lpsc2025/pdf/1236.pdf>

McMullan, S., & Collins, G. S. (2019, July). Uncertainty quantification in con-

tinuous fragmentation airburst models. *Icarus*, 327, 19–35. Retrieved 2024-08-16, from <https://www.sciencedirect.com/science/article/pii/S001910351830486X> doi: 10.1016/j.icarus.2019.02.013

Nakamura, T., Matsumoto, M., Amano, K., Enokido, Y., Zolensky, M. E., Mikiuchi, T., ... Tsuda, Y. (2022, September). Formation and evolution of carbonaceous asteroid Ryugu: Direct evidence from returned samples. *Science*, 379(6634), eabn8671. Retrieved 2025-11-14, from <https://www.science.org/doi/10.1126/science.abn8671> (Publisher: American Association for the Advancement of Science) doi: 10.1126/science.abn8671

Neal, R. M. (2003, June). Slice sampling. *The Annals of Statistics*, 31(3), 705–767. Retrieved 2025-04-16, from <https://projecteuclid.org/journals/annals-of-statistics/volume-31/issue-3/Slice-sampling/10.1214/aos/1056562461.full> (Publisher: Institute of Mathematical Statistics) doi: 10.1214/aos/1056562461

Neder, H., Laubenstein, M., & Heusser, G. (2001, September). Radionuclide Concentrations in the Freshly Fallen Meteorite Moravka. *Meteoritics and Planetary Science Supplement*, 36, A146. Retrieved 2025-04-17, from <https://ui.adsabs.harvard.edu/abs/2001M&PSA..36R.146N> (ADS Bibcode: 2001M&PSA..36R.146N)

Nemtchinov, I. (1994). Assessment of the 1 February 1994 Event. *Sandia National Labs*.

Ostrowski, D., & Bryson, K. (2019, January). The physical properties of meteorites. *Planetary and Space Science*, 165, 148–178. Retrieved 2025-11-13, from <https://www.sciencedirect.com/science/article/pii/S0032063318301843> doi: 10.1016/j.pss.2018.11.003

Picone, J. M., Hedin, A. E., Drob, D. P., & Aikin, A. C. (2002). NRLMSISE-00 empirical model of the atmosphere: Statistical comparisons and scientific issues. *Journal of Geophysical Research: Space Physics*, 107(A12), SIA 15–1–SIA 15–16. Retrieved 2025-11-12, from <https://onlinelibrary.wiley.com/doi/abs/10.1029/2002JA009430> (.eprint: <https://agupubs.onlinelibrary.wiley.com/doi/pdf/10.1029/2002JA009430>) doi: 10.1029/2002JA009430

Popova, O., Borovička, J., & Campbell-Brown, M. (2019). Modelling the entry of meteoroids. In A. D. J. Ryabova G. O. and Campbell-Brown M. D (Ed.), *Meteoroids: Sources of Meteors on Earth and Beyond* (Vol. 25, pp. 9–9). Cambridge University Press.

Popova, O., Borovička, J., Hartmann, W. K., Spurný, P., Gnos, E., Nemtchinov, I., & Trigo-Rodríguez, J. M. (2011). Very low strengths of interplanetary meteoroids and small asteroids. *Meteoritics & Planetary Science*, 46(10), 1525–1550. Retrieved 2025-05-28, from <https://onlinelibrary.wiley.com/doi/abs/10.1111/j.1945-5100.2011.01247.x> (.eprint: <https://onlinelibrary.wiley.com/doi/pdf/10.1111/j.1945-5100.2011.01247.x>) doi: 10.1111/j.1945-5100.2011.01247.x

Popova, O. P., Jenniskens, P., Emel'yanenko, V., Kartashova, A., Biryukov, E., Khaibrakhmanov, S., ... (the Chelyabinsk Airburst Consortium) (2013, November). Chelyabinsk Airburst, Damage Assessment, Meteorite Recovery, and Characterization. *Science*, 342(6162), 1069–1073. Retrieved 2025-01-14, from <https://www.science.org/doi/10.1126/science.1242642> doi: 10.1126/science.1242642

ReVelle, D. O. (2004, December). Recent Advances in Bolide Entry Modeling: A Bolide Potpourri. *Earth Moon and Planets*, 95, 441–476. Retrieved 2025-04-10, from <https://ui.adsabs.harvard.edu/abs/2004EM&P...95..441R> (Publisher: Springer ADS Bibcode: 2004EM&P...95..441R) doi: 10.1007/s11038-005-9064-4

Schwarz, G. (1978, March). Estimating the Dimension of a Model. *The Annals of*

Statistics, 6(2), 461–464. Retrieved 2025-04-15, from <https://projecteuclid.org/journals/annals-of-statistics/volume-6/issue-2/Estimating-the-Dimension-of-a-Model/10.1214/aos/1176344136.full> (Publisher: Institute of Mathematical Statistics) doi: 10.1214/aos/1176344136

Šrbený, L., Spurný, P., & Borovička, J. (2020, May). Fireball fragmentation in the first half of the atmospheric trajectory. *Planetary and Space Science*, 104956–104956. Retrieved from <https://doi.org/10.1016/j.pss.2020.104956> (Publisher: Elsevier Ltd) doi: 10.1016/j.pss.2020.104956

Silber, E. A., Le Pichon, A., & Brown, P. G. (2011, June). Infrasonic detection of a near-Earth object impact over Indonesia on 8 October 2009. *Geophysical Research Letters*, 38(12), 3–7. Retrieved from <http://www.agu.org/pubs/crossref/2011/2011GL047633.shtml> doi: 10.1029/2011GL047633

Simon, S. B., Grossman, L., Clayton, R. N., Mayeda, T. K., Schwade, J. R., Sipiera, P. P., ... Wadhwa, M. (2004). The fall, recovery, and classification of the Park Forest meteorite. *Meteoritics & Planetary Science*, 39(4), 625–634. Retrieved 2025-04-19, from <https://onlinelibrary.wiley.com/doi/abs/10.1111/j.1945-5100.2004.tb00925.x> (eprint: <https://onlinelibrary.wiley.com/doi/pdf/10.1111/j.1945-5100.2004.tb00925.x>) doi: 10.1111/j.1945-5100.2004.tb00925.x

Skilling, J. (2004). Nested Sampling. In *AIP Conference Proceedings* (Vol. 735, pp. 395–405). Garching (Germany): AIP. Retrieved 2025-03-24, from <https://pubs.aip.org/aip/acp/article/735/1/395-405/748716> (ISSN: 0094243X) doi: 10.1063/1.1835238

Skilling, J. (2006, December). Nested sampling for general Bayesian computation. *Bayesian Analysis*, 1(4), 833–859. Retrieved 2025-03-24, from <https://projecteuclid.org/journals/bayesian-analysis/volume-1/issue-4/Nested-sampling-for-general-Bayesian-computation/10.1214/06-BA127.full> (Publisher: International Society for Bayesian Analysis) doi: 10.1214/06-BA127

Speagle, J. S. (2020, April). dynesty: a dynamic nested sampling package for estimating Bayesian posteriors and evidences. *Monthly Notices of the Royal Astronomical Society*, 493(3), 3132–3158. Retrieved 2025-03-24, from <https://doi.org/10.1093/mnras/staa278> doi: 10.1093/mnras/staa278

Spurný, P., Borovička, J., Šrbený, L., Hankey, M., & Neubert, R. (2024, June). Atmospheric entry and fragmentation of the small asteroid 2024 BX1: Bolide trajectory, orbit, dynamics, light curve, and spectrum. *Astronomy & Astrophysics*, 686, A67. Retrieved 2025-03-24, from <https://www.aanda.org/articles/aa/abs/2024/06/aa49735-24/aa49735-24.html> (Publisher: EDP Sciences) doi: 10.1051/0004-6361/202449735

Svetsov, V. V., Nemtchinov, I. V., & Teterev, A. V. (1995, July). Disintegration of Large Meteoroids in Earth's Atmosphere: Theoretical Models. *Icarus*, 116(1), 131–153. Retrieved 2025-06-10, from <https://www.sciencedirect.com/science/article/pii/S0019103585711165> doi: 10.1006/icar.1995.1116

Tagliaferri, E., Spalding, R., Jacobs, C., & Ceplecha, Z. (1995, January). Analysis of the Marshall Islands Fireball of February 1, 1994. *Earth, Moon, and Planets*, 68(1-3), 563–572. Retrieved 2024-09-06, from <https://link.springer.com/10.1007/BF00671553> doi: 10.1007/BF00671553

Tárano, A. M., Wheeler, L. F., Close, S., & Mathias, D. L. (2019, September). Inference of meteoroid characteristics using a genetic algorithm. *Icarus*, 329, 270–281. Retrieved 2024-09-23, from <https://www.sciencedirect.com/science/article/pii/S0019103518305669> doi: 10.1016/j.icarus.2019.04.002

Unsalan, O., Jenniskens, P., Yin, Q.-Z., Kaygisiz, E., Albers, J., Clark, D. L., ... Consortium, T. S. M. (2019). The Sarıçık howardite fall in Turkey: Source crater of HED meteorites on Vesta and impact risk of Vestaoids. *Meteoritics & Planetary Science*, 54(5), 953–1008. Retrieved 2024-06-29, from

<https://onlinelibrary.wiley.com/doi/abs/10.1111/maps.13258> doi: 10.1111/maps.13258

Vida, D., Brown, P. G., Devillepoix, H. A. R., Wiegert, P., Moser, D. E., Matlovič, P., ... Hladiuk, D. W. (2023, March). Direct measurement of decimetre-sized rocky material in the Oort cloud. *Nature Astronomy*, 7(3), 318–329. Retrieved 2024-09-24, from <https://www.nature.com/articles/s41550-022-01844-3> (Publisher: Nature Publishing Group) doi: 10.1038/s41550-022-01844-3

Wheeler, L. F., Mathias, D. L., Stokan, E., & Brown, P. G. (2018, November). Atmospheric energy deposition modeling and inference for varied meteoroid structures. *Icarus*, 315, 79–91. Retrieved 2024-08-08, from <https://linkinghub.elsevier.com/retrieve/pii/S0019103518301313> doi: 10.1016/j.icarus.2018.06.014

Wheeler, L. F., Register, P. J., & Mathias, D. L. (2017, October). A fragment-cloud model for asteroid breakup and atmospheric energy deposition. *Icarus*, 295, 149–169. Retrieved 2024-08-06, from <https://www.sciencedirect.com/science/article/pii/S0019103516307989> doi: 10.1016/j.icarus.2017.02.011

Wisniewski, K. S., Brown, P. G., Moser, D. E., & Longenbaugh, R. (2024, July). Determining the population of large meteoroids in major meteor showers. *Icarus*, 417, 116118. Retrieved 2024-11-24, from <https://www.sciencedirect.com/science/article/pii/S0019103524001787> doi: 10.1016/j.icarus.2024.116118